

Understanding the resilient carbon cycle response to the 2014–2015 Blob event in the Gulf of Alaska using a regional ocean biogeochemical model

Yumi Abe¹, Takamitsu Ito¹, Amanda H. V. Timmerman², Christopher T. Reinhard¹, Joseph P. Montoya³

¹School of Earth and Atmospheric Sciences, Georgia Institute of Technology, Atlanta, 30332-0340, U.S.A.

²Virginia Institute of Marine Science, Gloucester Point, 23062-1346, U.S.A.

³School of Biological Sciences, Georgia Institute of Technology, Atlanta, 30332-0230, U.S.A.

Correspondence to: Yumi Abe (yumiabe@gatech.edu)

Abstract. Marine heatwaves (MHWs), characterized by anomalously high sea surface temperatures, are increasing in frequency and intensity and strongly impact ocean circulation, biogeochemistry, and marine ecosystems. During the 2014–2015 MHW (commonly called the Blob) in the NE subarctic northeastern-Pacific, moored observations at Ocean Station Papa (OSP; 145°W, 50°N) showed a moderate decrease in oceanic pCO₂, contrary to the increase expected from warming-induced solubility reduction alone. Using a regional model that reproduces the observed pCO₂ variability and trend at OSP, we show that this decline resulted from a decrease in reduced-dissolved inorganic carbon (DIC) supply that outweighed the warming-driven increase in pCO₂. The DIC reduction was primarily caused by weakened vertical transport associated with enhanced upper-ocean stratification and reduced Ekman pumping prior to the onset of the Blob, which suppressed the upwelling of DIC-rich subsurface waters. Horizontal transport also contributed locally, particularly at OSP. These results demonstrate that anomalous physical circulation, rather than biological processes, was the primary driver of the enhanced CO₂ uptake during the Blob and highlight the importance of resolving physical transport mechanisms when assessing carbon cycle responses to extreme warming events.
~~Marine heatwaves (MHWs), characterized by anomalously high sea surface temperatures, are occurring with increasing frequency and intensity, profoundly impacting ocean circulation, biogeochemistry, and marine ecosystems. The MHW known as the Blob, which persisted in the subarctic NE Pacific from 2014 to 2015, significantly affected surrounding ecosystems. Warming induced solubility reduction is expected to raise the partial pressure of carbon dioxide (pCO₂) in the surface water, causing outgassing of CO₂ to the atmosphere. Outgassing of CO₂ is another source of atmospheric CO₂ in addition to anthropogenic fossil fuel burning. However, moored observations at Ocean Station Papa (OSP; 145°W, 50°N) shows a moderate decrease in oceanic pCO₂ during the Blob, resisting the warming induced outgassing of CO₂. This response is opposite of what is expected from warming alone, and instead has been attributed to reductions in dissolved inorganic carbon (DIC), although the mechanisms driving this reduction have remained unclear. We employed a regional~~

30 model that accurately reproduces the temporal variability of oceanic pCO₂ at OSP to investigate the cause of decrease pCO₂
31 during the Blob. The analysis of model outputs indicates that the observed oceanic pCO₂ decline resulted from the offset
32 between warming induced solubility reduction (increasing pCO₂) and weakened physical transport of DIC (decreasing pCO₂),
33 with the latter dominating. Both horizontal and vertical transports played important roles. The near-surface carbon budget over
34 the broad region was primarily driven by changes in the vertical transport. The decrease in DIC during the Blob resulted from
35 the suppression of upwelling of DIC rich subsurface waters in the winter of 2013. In this period, the horizontal transport also
36 contributed substantially to DIC reduction. In particular, at OSP, the effect of the horizontal transport was comparable to that
37 of the vertical transport, reflecting the northward advection of low-DIC water masses. These findings indicate that changes in
38 physical circulation were the primary driver of the moderately enhanced CO₂ uptake observed during the Blob. This study
39 provides a critical insight into the complexity of biogeochemical response to extreme warming events and underscores the
40 importance of resolving physical transport processes in assessing oceanic carbon uptake during MHWs.

41 1 Introduction

42 Approximately 25% of historical anthropogenic carbon emission has been absorbed by the oceans (Friedlingstein et al., 2022),
43 and the North Pacific is one of the major regions for ocean carbon uptake (Takahashi et al., 2009). The carbon exchange
44 between the atmosphere and ocean is closely related to ocean temperature through its influences on the solubility of carbon
45 dioxide (CO₂) in seawater. In recent years, anomalously high ocean temperatures ~~are frequently observed~~, known as marine
46 heatwaves (MHWs; Hobday et al., 2016). have been frequently observed. These events are defined by prolonged periods of
47 unusually high sea surface temperature (SST) anomalies and their intensity. With the ongoing progression of global warming,
48 the frequency and intensity of MHWs have been increasing (Frölicher et al., 2018; Oliver et al., 2018). In particular, the
49 persistent MHW that occurred in the subarctic NE Pacific from the winter of 2013 to 2015, known as *the Blob* (Bond et al.,
50 2015), had severe impacts on surrounding ecosystems (Cavole et al., 2016; Smale et al., 2019) and fisheries (Barbeaux et al.,
51 2020). This anomalously high ocean temperature was attributed to weaker surface winds, which reduced ocean surface heat
52 loss, and weakened horizontal and vertical mixing (Bond et al., 2015; Di Lorenzo and Mantua, 2016).

53
54 Biogeochemical variables are also impacted by MHWs. In particular, low-oxygen and acidification become more pronounced
55 during MHWs (Gruber et al., 2021; Burger et al., 2022; Li et al., 2024b). These changes are driven by alterations in ocean
56 circulation due to changes in driven by winds and air-sea interactions associated with atmospheric anomalies that induce the
57 MHWs, and also by the direct effects of high temperatures (e.g., including enhanced stratification, reduced solubility, and
58 changes in biological activity). During the Blob, both surface dissolved oxygen and inorganic carbon (DIC) were significantly
59 decreased partly due to reduced solubility caused by increased rising water temperatures (Mogen et al., 2022; based on ocean
60 model outputs from NorESM and MRI simulations).- Franco et al. (2021) showed a decrease in surface DIC during the Blob

61 ~~using Consistent with this, in situ time-series measurements (Franco et al., 2021) also show a declining trend in surface DIC~~
62 ~~during the Blob.~~

63
64 For the air–sea CO₂ exchange, the uptake in the North Pacific decrease~~d~~s by 29±11% during persistent MHWs mainly due to
65 the direct effect of increase~~d~~ in water temperature (Mignot et al., 2022). However, this reduction in ocean carbon uptake is
66 primarily driven by the substantial increase in oceanic CO₂ outgassing in the tropical Pacific. Focusing on the subarctic regions,
67 the oceanic CO₂ uptake increase~~d~~s during the MHWs. For example, mooring data from Ocean Station Papa (OSP; 50°N,
68 145°W) in the eastern North Pacific, which is one of the longest-running observation sites, ~~showed~~ indicate the low surface
69 DIC and oceanic partial pressure of CO₂ (pCO₂) during a more recent MHW (Kohlman et al., 2024). In the Gulf of Alaska
70 (GOA), air–sea CO₂ flux exhibited a negative anomaly (stronger ocean uptake) of approximately 45% relative to the
71 climatological monthly means during the Blob based on a machine-learning based reconstruction (Duke et al., 2023). The
72 enhanced ocean carbon uptake is caused by the decrease in oceanic pCO₂ in the subarctic North Pacific, which is driven by the
73 effects of reduced surface ocean DIC. However, the processes responsible for this DIC reduction is not fully understood
74 (Mignot et al., 2022; Li et al., 2024a). Furthermore, estimates of oceanic pCO₂ changes derived from observation-based
75 products are subject to considerable uncertainty, as observational data in the subarctic North Pacific are temporally and
76 spatially sparse. Consequently, discrepancies among data products restrict the robustness of their assessments (Li et al., 2024a).

77
78 To elucidate the mechanisms by which the MHWs lead to the observed changes in oceanic pCO₂ and air–sea CO₂ fluxes,
79 numerical models can provide the carbon mass balance and exploring underlying physical and biogeochemical processes.
80 Physical processes that control the regional ocean circulation, biogeochemical cycling, and air–sea gas exchanges often occur
81 at scales smaller than several tens of kilometres, which remain unresolved in global earth system models (Gruber et al., 2021).
82 In the subarctic NE Pacific, reproducing the full variability of oceanic pCO₂ in models is complicated by boundary currents
83 and eddies that transport macro- and micro-nutrients, alkalinity and DIC. A previous study using a coarse resolution model
84 (Mckinley et al., 2006) has shown that although models captured the variability of individual components of oceanic pCO₂ on
85 seasonal and interannual timescales, they have not fully reproduced the total variability of oceanic pCO₂, and their ability to
86 simulate the temporal patterns of air–sea CO₂ fluxes remains limited.

87
88 There are several regional modeling studies exploring biogeochemical processes in the GOA. Coyle et al. (2012) developed
89 regional, biogeochemical simulations for the northern GOA based on the ROMS circulation model with the horizontal
90 resolution of 3 km from 2001 to 2004 focusing on the coastal regions. The biogeochemical model component is based on the
91 GOANPZ model (Hinckley et al., 2009). The model reproduced the spring phytoplankton bloom from the continental shelves
92 to the open ocean. This model subsequently was used to analyze ocean acidification with the inclusion of carbonate chemistry
93 (Siedlecki et al., 2017). Hauri et al. (2020) developed a hindcast simulation for the similar northern GOA domain. They also
94 used the ROMS physical model with 4.5 km horizontal resolution. The biogeochemical component is based on the COBALT

95 biogeochemistry model (Stock et al., 2014) with specific modifications to capture coastal ecosystems. Following these previous
96 studies, we constructed a regional biogeochemical and carbon cycle model for the GOA. The model has been validated against
97 a suite of physical and biogeochemical observations (Ito et al., 202~~65~~) This study expands the model to include a validated
98 carbon cycle component. The simulated temporal variability of oceanic pCO₂ is validated with the NOAA (Pacific Marine
99 Environmental Laboratory’s Ocean Climate Stations and Carbon groups) mooring at OSP (Emerson et al., 2011; Cronin et al.,
100 2015). The model outputs are used to understand the underlying mechanisms and to quantify the changes in oceanic pCO₂ in
101 this critical carbon sink during the Blob. This paper includes the description of the model and the observational data used for
102 model validation (section 2), and the results of oceanic pCO₂ variations during the Blob and its causes (section 3). Section 4
103 discusses the associated changes in CO₂ flux, the potential impacts of high ocean temperature anomalies on the regional carbon
104 cycle, their effects on the broader ocean basin, and possible future implications. Finally, Section 5 summarizes the main
105 findings of this study.~~Conclusions and discussion (section 4) summarizes this study with the potential impacts of high ocean~~
106 ~~temperature anomalies on regional carbon cycle, their effects on the wider ocean basin, and possible future implications~~
107 ~~(section 4).~~

108 **2 Data and Methods**

109 **2.1 Model description**

110 The regional ocean circulation and biogeochemistry model used in this study follow~~eds~~ the configuration described in Ito et
111 al. (202~~65~~), thus only a brief description was~~is~~ provided here, while full details can be found in their paper. The model was~~is~~
112 based on MITgcm (Marshall et al., 1997a, b) combined with an ocean biogeochemical model, Biogeochemistry with Light,
113 Iron, Nutrients and Gases (BLING) version 2 (Dunne et al., 2020) including 10 tracers, DIC, alkalinity, O₂, PO₄, NO₃, dissolved
114 Fe, silica, dissolved organic P, and dissolved organic N. The model was~~is~~ driven by 3-hourly averaged atmospheric variables
115 from the JRA-55-do reanalysis data (T sujino et al., 2018), including the surface air temperature, humidity, 10 m wind stress,
116 precipitation (both rain and snow), river runoff, and downward shortwave and longwave radiation. The earlier simulations of
117 Ito et al. (202~~65~~) included a positive bias in sea surface salinity (SSS) of approximately +0.2 psu. To maintain SSSs close to
118 the observations, we applied Newtonian relaxation to SSS toward monthly climatology from World Ocean Atlas 2023 (Reagan
119 et al., 2024) with a restoring timescale of 30 days in the surface grid box of 10 m thickness. The model ha~~ds~~ a horizontal
120 resolution of 10 km with 42 vertical layers on a latitude-longitude z-level grid. The bathymetry was generated by interpolating
121 the ETOPO2 global 2-minute resolution topography dataset. The model domain ha~~ds~~ a southern open boundary at 42°N and a
122 western open boundary at 160°W. Vertical mixing was parameterized using the K-profile Parameterization (KPP) scheme
123 (Large et al., 1994) as implemented in MITgcm. The default configuration, including the non-local convection term, was used
124 for this study. KPP diffusivities were applied to momentum and all tracers. A sea ice model, implemented using the MITgcm
125 sea ice package (Losch et al., 2010) and coupled to the ocean component, was used to represent sea ice dynamics and
126 thermodynamics, as well as their influence on surface heat, freshwater, and momentum fluxes.

127

128 Both the initial and boundary conditions in our model also followed Ito et al. (2026~~5~~). Open boundary conditions ~~were~~ set
129 to the climatological values from GLODAPv2 (Lauvset et al., 2022) for most of the biogeochemical properties. However, for
130 DIC, the open boundary conditions included time-dependent anthropogenic carbon rather than climatology. Temporal changes
131 in DIC due to anthropogenic influences ~~were~~ imposed according to the rate of change in atmospheric CO₂ fractions
132 measured at the Mauna Loa Observatory (Keeling et al., 2001) and its spatial structure ~~was~~ set to the anthropogenic carbon
133 estimates from the GLODAPv2. The model integration was performed through 2017, and the physical open boundary
134 conditions were taken from the oceanic reanalysis data of Simple Ocean Data Assimilation (SODA) version 3 (Carton and
135 Giese, 2008; Carton et al., 2018).

136

137 Several biogeochemical parameters were adjusted to improve the model representation of the carbon cycle. These
138 modifications primarily involved processes related to strength of photosynthesis and remineralization. The modeled default
139 parameters for photosynthetic rates caused excessively high rates in coastal waters, resulting in unrealistically elevated primary
140 production. To address this, the self-shading effect of phytoplankton ~~was~~ turned on, which regulated the light available for
141 phytoplankton growth in the highly productive coastal waters. The bio-optical parameterization of Manizza et al. (2005) ~~was~~
142 used in our configuration but the background attenuation coefficient in this bio-optical model was reduced to one-quarter of
143 its default value to re-calibrate the net primary production (NPP). Furthermore, the simulated oceanic pCO₂ ~~was~~ highly
144 sensitive to the production of organic matter and the subsequent remineralization. A key factor ~~was~~ the export ratio which
145 determines the fraction of NPP that sinks as particulate organic matter from the surface layer and ~~was~~ subsequently
146 recycled in the subsurface waters. Among the relevant parameters, the partitioning of particulate organic versus dissolved
147 organic matter exerted a particularly strong influence on the representation of oceanic pCO₂. To better capture observed
148 oceanic pCO₂, we adjusted this parameter so that 30% of NPP is converted to dissolved organic matter, compared with a
149 default value of 10%, which means that more organic matter ~~was~~ recycled in the surface layer than the default configuration.

150 2.2 Observations

151 To evaluate the model skills in reproducing the observed oceanic pCO₂, SeaFlux data (Fay et al., 2021) ~~were~~ used for spatial
152 comparisons, and NOAA CO₂ mooring data (Emerson et al., 2011; Cronin et al., 2015) ~~were~~ used for temporal comparisons
153 at OSP. SeaFlux data consisted of six global observation-based gridded products that reconstruct spatiotemporally continuous
154 estimates of air-sea CO₂ fluxes using different gap-fill methods on the surface oceanic pCO₂ observations. Because the spatial
155 resolution of SeaFlux ~~was~~ one degree in latitude and longitude, our model output was remapped to the same resolution using
156 nearest-neighbour interpolation for comparison. In June 2007, a surface CO₂ mooring time series was initiated at OSP by S.
157 Emerson for the study of North Pacific Carbon Cycle, and the mooring observation has been continued by NOAA Office of
158 Climate Observations. This data provided both physical and biogeochemical variables. For comparison with the model,
159 temperature, salinity, and both oceanic and atmospheric pCO₂ data were obtained from the mooring dataset archived at

160 https://www.ncei.noaa.gov/access/ocean-carbon-acidification-data-system/oceans/Moorings/Papa_145W_50N.html (last
161 access: 1 Oct 2025). For comparison, OSP in the model was represented by averaging all grid points within a 24 km radius of
162 50°N, 145°W.

163
164 Model skill wasis further evaluated against the spatial patterns of monthly SST anomalies from the OISST dataset (0.25°
165 resolution; Reynolds et al., 2007; Huang et al., 2021) and the HadISST dataset (1° resolution; Rayner et al., 2003).

166 2.3 Analysis methods

167 The oceanic pCO₂ anomalies ~~wereare~~ decomposed as:

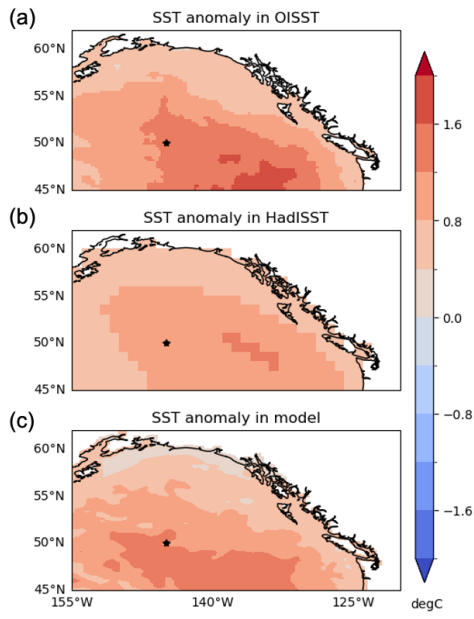
$$169 \delta pCO_2 \approx \frac{\partial pCO_2}{\partial T} \delta T + \frac{\partial pCO_2}{\partial S} \delta S + \frac{\partial pCO_2}{\partial DIC^*} \delta DIC^* + \frac{\partial pCO_2}{\partial ALK^*} \delta ALK^* \#(1)$$

170
171 where oceanic pCO₂ ~~wasis~~ a function of ~~sea surface temperature (SST; T)~~, SSS (S), sea surface salinity-normalized DIC
172 (DIC*) and sea surface salinity-normalized alkalinity (ALK*). The contributions of these four variables to the oceanic pCO₂
173 anomalies ~~wereare~~ calculated using the Python toolbox PyCO2SYS (Humphreys et al., 2022) version 1.8.3. For the input
174 variables, DIC and alkalinity were normalized to a salinity of 35 to eliminate the influence from evaporation and dilution
175 (Keeling et al., 2004). The partial derivatives were evaluated at each time step by perturbing each variable independently while
176 holding the others constant. For this calculation, the constants were set to the median of the temporal variations, and the
177 perturbations were applied with an amplitude equal to the standard deviation. The results were obtained for each grid, and the
178 values at OSP were as follows: $\partial pCO_2 / \partial T = 15.27 \mu atm / ^\circ C$, $\partial pCO_2 / \partial S = 25.26 \mu atm / psu$, $\partial pCO_2 / \partial DIC^* = 2.15 \mu atm /$
179 $\mu mol kg^{-1}$, $\partial pCO_2 / \partial ALK^* = -1.76 \mu atm / \mu mol kg^{-1}$. In the oceanic pCO₂ decomposition analysis, all input variables
180 were detrended and deseasonalized using the STL function from the statsmodels.tsa.seasonal module in Python.

181 3 Results

182 3.1 Observational evidence of ΔpCO_2 during marine heatwave

183 To assess the magnitude of the SST anomalies during the Blob and evaluate whether the model wasis consistent with the
184 observations, we ~~first~~ compared the observed SST anomaly fields (Fig. 1). Both OISST and HadISST showed positive
185 temperature anomalies across the GOA. The SST anomalies in OISST ~~wereare~~ larger than those in HadISST, particularly in
186 the southeastern region. The modeled SST anomalies showed good agreement with both OISST and HadISST in terms of their
187 spatial patterns and overall amplitudes. Given this consistency, the model robustly representeds the observed SST anomalies,
188 suggesting that model biases in SST ~~wereare~~ unlikely to influence the interpretation of the SST-driven component of oceanic
189 pCO₂.



190

191 Figure 1: Annual SST anomaly during Blob (2014–2015) relative to 2010–2017 from (a) OISST, (b) HadISST, and (c) the
 192 model. The star indicates where the location of OSP is located.

193

194 Seaflux pCO₂ data revealed the basin-scale surface oceanic pCO₂ climatologies and anomalies during the Blob. Annual mean
 195 climatology (2010–2017) shows negative $\Delta p\text{CO}_2$ (oceanic pCO₂ is smaller than the atmospheric pCO₂), indicating that the
 196 entire domain of the model region acts as a sink for atmospheric CO₂ in the climatological mean field indicating that the
 197 GOA is on average a sink of atmospheric CO₂ (Fig. 21a). Positive SST anomalies were expected to reduce CO₂ saturation
 198 in the ocean and consequently increase oceanic pCO₂. However, observation-based data showed a decrease in oceanic pCO₂,
 199 accompanied by a larger amplitude of $\Delta p\text{CO}_2$ than non-heatwave conditions during the Blob (Fig. 2c). This indicates that the
 200 surface ocean absorbed more CO₂ from the atmosphere during the Blob (2014–2015), and is especially evident in the central
 201 GOA (blue areas in Fig. 21b, c). This trend contrasted with the rising SST, which increases oceanic pCO₂ and reduces ocean
 202 carbon uptake (Fig. 2d). This trend is at odds against the rising SST, which tends to increase the oceanic pCO₂ and reduce
 203 ocean carbon uptake (Fig. 1d). An estimated contribution from the positive SST anomalies on indicates that $\Delta p\text{CO}_2$ should
 204 result in an increase in $\Delta p\text{CO}_2$ across the entire region (Fig. 21d). Therefore, elevated SST cannot account for the observed
 205 decrease in $\Delta p\text{CO}_2$ during the Blob.

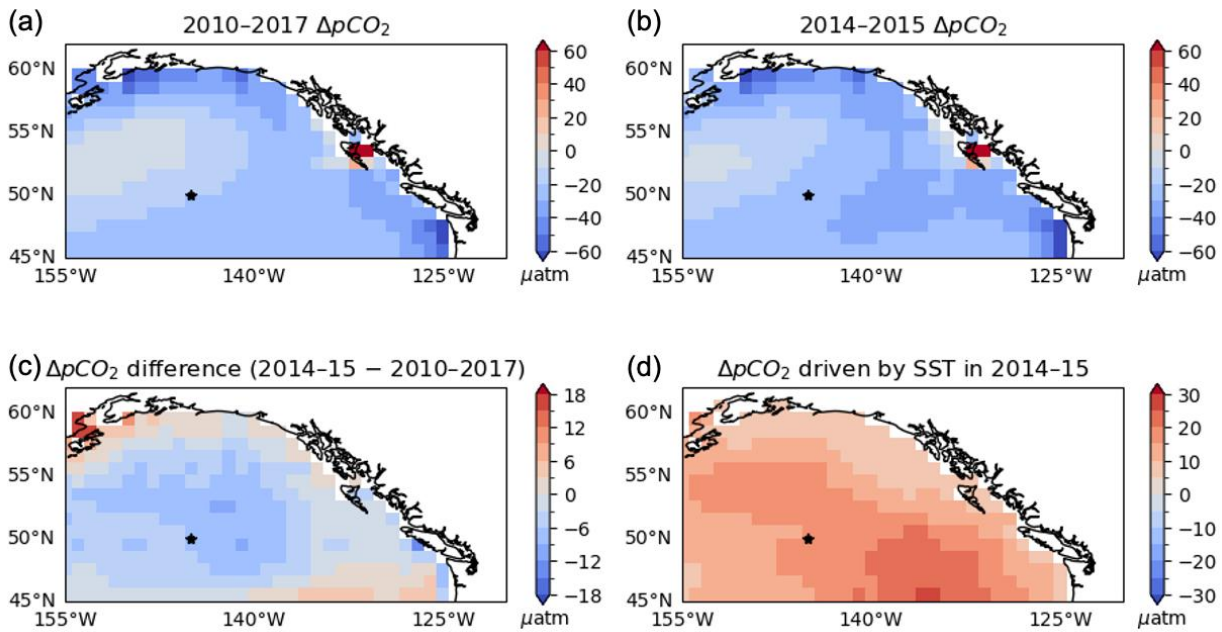
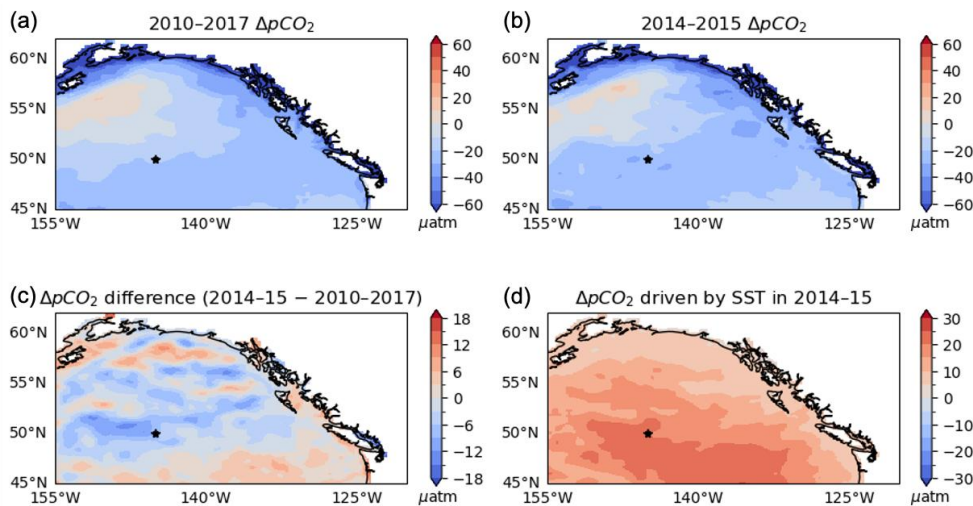


Figure 24: $\Delta p\text{CO}_2$ (oceanic $p\text{CO}_2$ minus atmospheric $p\text{CO}_2$): (a) mean over 2010–2017, (b) mean during the Blob period from 2014–2015, (c) difference between (b) and (a), and (d) the component driven by SST changes during the Blob in SeaFlux. The SST-driven oceanic $p\text{CO}_2$ in (d) is calculated as the difference between $p\text{CO}_2$ computed under climatological mean conditions (2010–2017 mean SST and SSS from SODA version 3.4.2, and DIC and alkalinity from GLODAPv2) and $p\text{CO}_2$ computed using SST from 2014–2015, while keeping the other variables fixed at their climatological values, with PyCO2SYS. Blue indicates CO_2 uptake by the ocean, and red indicates CO_2 outgassing to the atmosphere. The star in each panel marks the location of OSP. The SST-driven oceanic $p\text{CO}_2$ in (d) driven is calculated as the difference between $p\text{CO}_2$ computed under climatological mean conditions (2010–2017 mean SST and SSS from SODA version 3.4.2, and DIC and alkalinity from GLODAPv2) and $p\text{CO}_2$ computed using SST from 2014–2015, while keeping the other variables fixed at their climatological values, with PyCO2SYS. $\Delta p\text{CO}_2$ (oceanic $p\text{CO}_2$ minus atmospheric $p\text{CO}_2$) comparison the Blob and climatology in SeaFlux. Blue shows CO_2 uptake, and red shows CO_2 outgassing. The star in each panel indicates the location of OSP. Oceanic $p\text{CO}_2$ driven by SST is calculated using SST from SODA version 3.4.2 and DIC and alkalinity from GLODAPv2.

3.2 Model validation

Before using the model to address the underlying mechanism behind the oceanic $p\text{CO}_2$ decreases during the Blob, the ability of the model to reproduce existing observations must be evaluated. We first examined the model output for $\Delta p\text{CO}_2$, the time-averaged oceanic $p\text{CO}_2$ in the GOA from 2010 to 2017. Consistent with the observations, the model indicated that increasing SST cannot account for the changes in oceanic $p\text{CO}_2$ under the Blob, not only at OSP but across the entire GOA (Fig. 3). Compared to the observations (Fig. 2), $\Delta p\text{CO}_2$ driven by SST under the Blob in the model was approximately $5 \mu\text{atm}$ higher around OSP. Despite the moderate overestimation in thermal-driven $p\text{CO}_2$ anomaly, the modeled $\Delta p\text{CO}_2$ showed a significant decrease across the central GOA, consistent with the SeaFlux dataset and the mooring observation at OSP. This consistency was underscoring the robustness of the modeled response. Throughout the region, the effect of warming-induced increase in the oceanic $p\text{CO}_2$ was offset by the oceanic $p\text{CO}_2$ reduction driven by decreased DIC, which was consistent with the previous work by Kohlman et al. (2024).

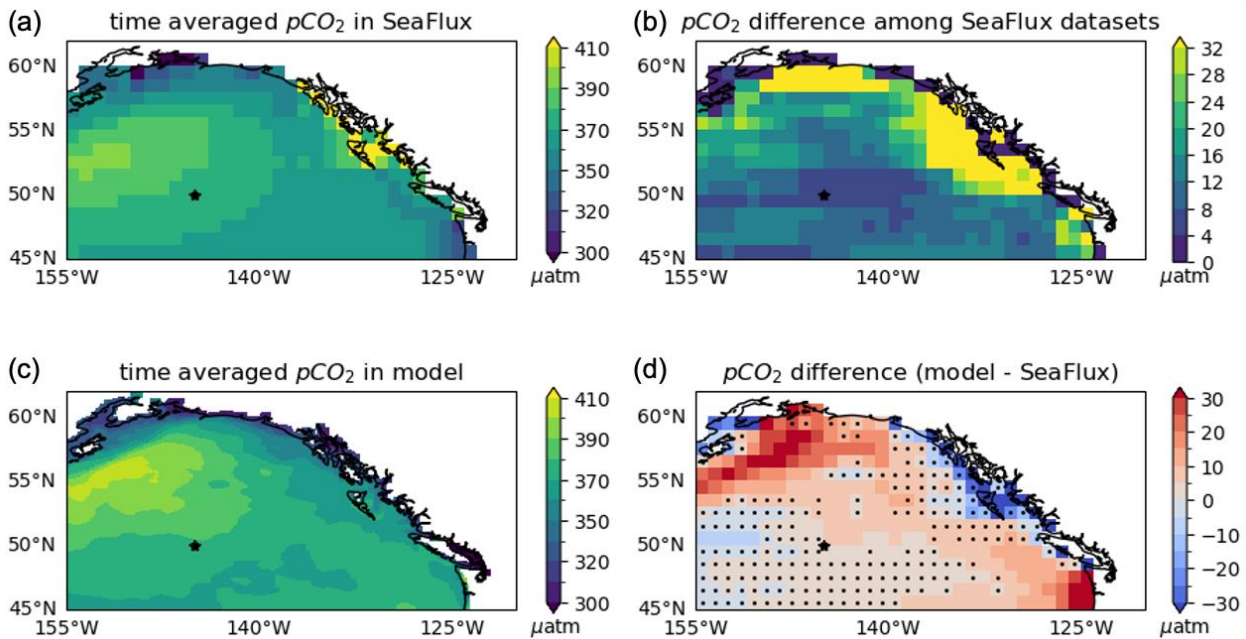


230

231 **Figure 3: Same as Fig. 2 but for the model results.**

232

233 Compared to the ensemble mean of the time-averaged oceanic pCO_2 from 2010 to 2017 in the SeaFlux dataset, the spatial
 234 correlation between SeaFlux and the model was moderately positive ($r=0.30$), and the model generally reproduced s the broad
 235 climatological spatial distribution of the observed SeaFlux oceanic pCO_2 (Fig. 432a, c). The model overestimated the oceanic
 236 pCO_2 in the northwestern area, which likely arised s from model circulation biases in this region. Compared to satellite
 237 observations, the model had s slightly weaker horizontal geostrophic flow, and the core of the subpolar circulation was shifted
 238 northward (Ito et al. 20265). The modeled vertical stratification was slightly weakened relative to the climatological
 239 observations, and this weak stratification bias led leads to a higher oceanic pCO_2 in the model. To evaluate the uncertainties
 240 in the SeaFlux dataset, variability among the different observational ensembles must be considered. In the open ocean, modeled
 241 oceanic pCO_2 was within the range of SeaFlux ensemble variability (Fig. 432b, d). Therefore, in most areas, the model was
 242 within the uncertainty bounds of the observation-based oceanic pCO_2 .



243

244

245

246

Figure 432: Comparison of oceanic $p\text{CO}_2$ distributions, averaged over 2010–2017, between the model and SeaFlux. The star in each panel indicates the location of OSP. Dots in (d) indicate the grid points where the modeled climatology falls within the range of differences among the SeaFlux ensemble datasets.

247

248

249

250

251

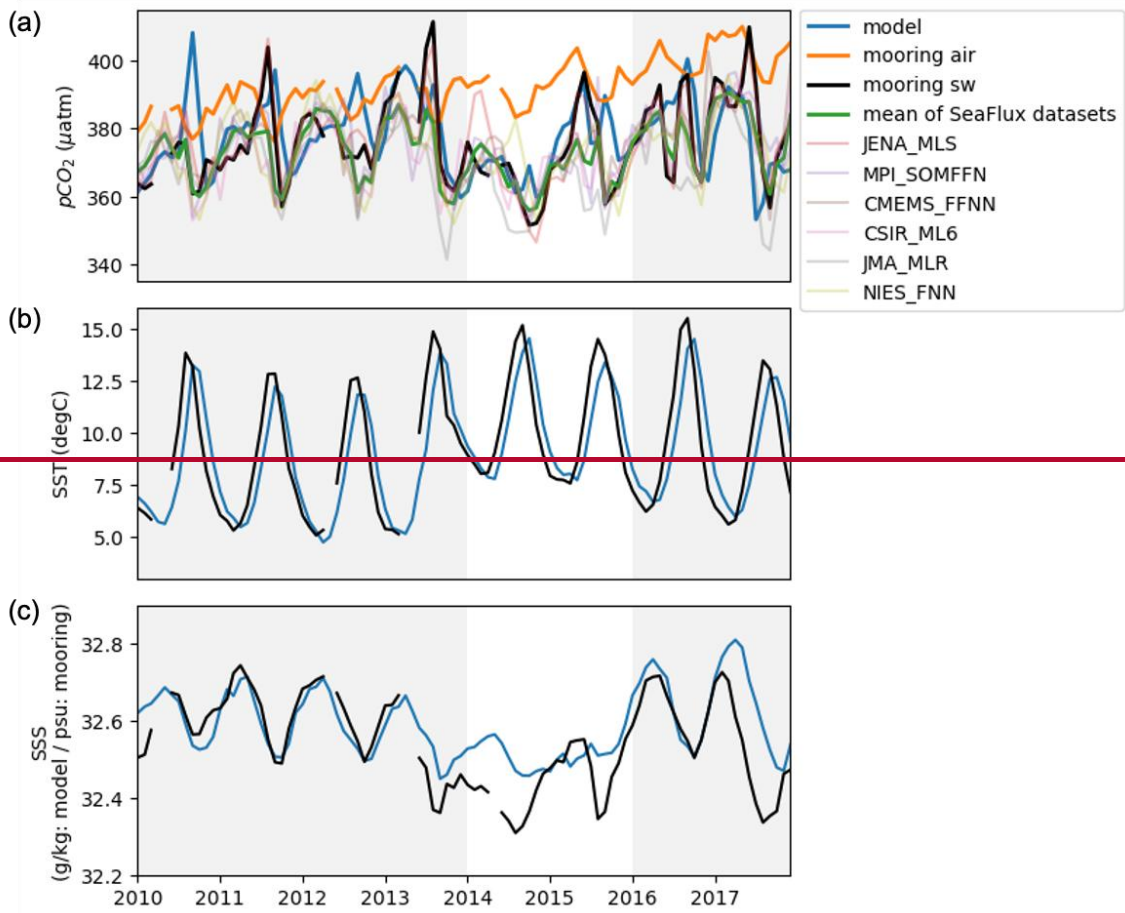
252

253

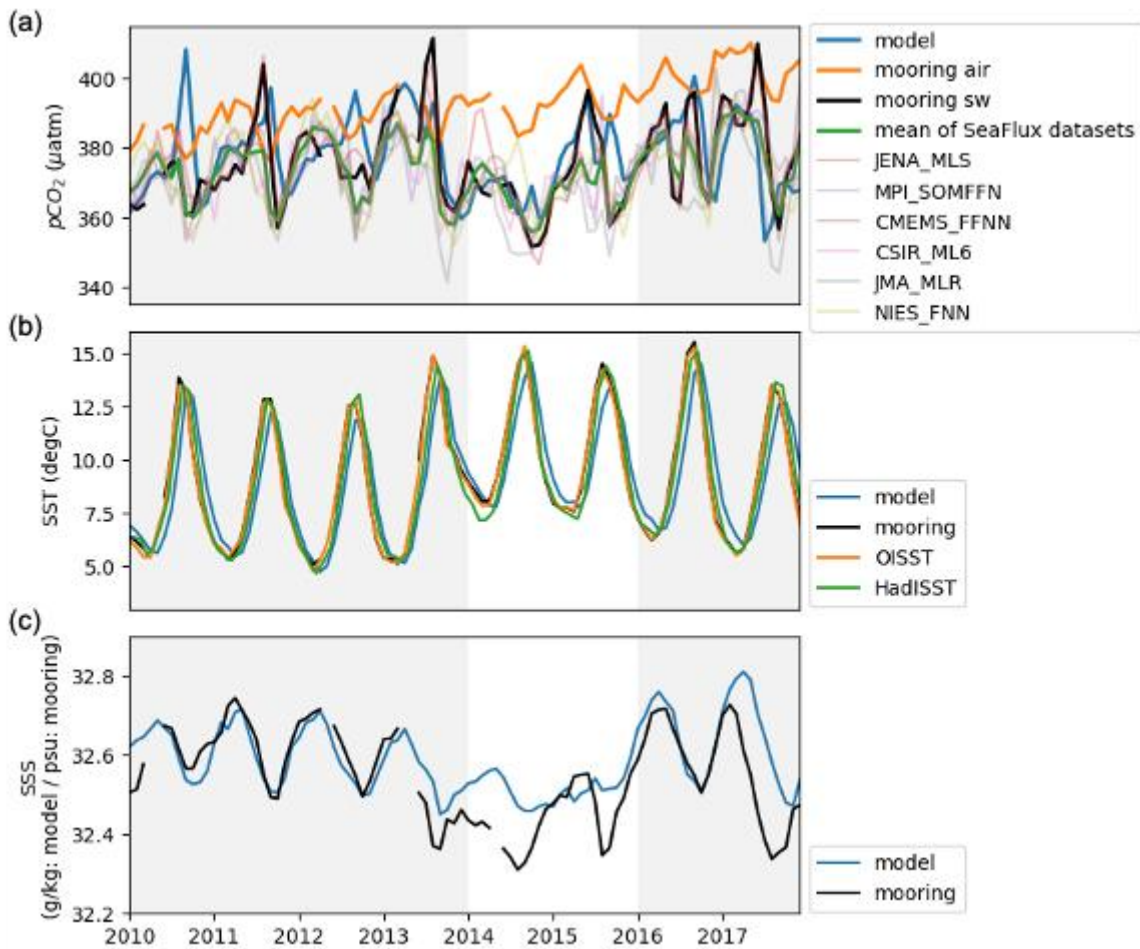
254

255

The model also reproduceds the temporal variation in oceanic $p\text{CO}_2$ to a reasonable extent. Compared with the mooring time series at OSP, the model captureds the observed variability and magnitude in both biogeochemical and physical variables (Fig. 543). For oceanic $p\text{CO}_2$, the model reproduce~~ds~~s a statistically significant fraction of the mooring $p\text{CO}_2$ variability ($r=0.44$, normalized-RMSE=1.01), and fellfalls within the spread of the SeaFlux ensemble data. During the Blo~~ub~~ub, both the mooring observations and model show~~ed~~ed pronounced decline in oceanic $p\text{CO}_2$. Correspondingly, $\Delta p\text{CO}_2$, which represent~~eds~~eds the difference between the black or blue line and the orange line in Fig. 43a also decrease~~ds~~ds. The model slightly overestimated SSS (~ 0.1 psu) compared to the mooring during the Blob, but this did~~does~~does not significantly compromise the stratification in the model, because the density wasis primarily governed by sea water temperature in this region.



256



257

258 **Figure 543:** Comparison of time series between the model and mooring observations at OSP for (a) oceanic pCO₂, (b) SST, and (c)
 259 SSS. In (a), atmospheric pCO₂ from the mooring observations is additionally shown in orange (mooring air) to illustrate variation
 260 in ΔpCO₂. Oceanic pCO₂ from the SeaFlux ensemble mean is also shown in green, with individual ensembles indicated by thin lines
 261 with different colors. In (b) and (c), the model is blue and mooring (seawater, sw) is black. **In (b), OISST is shown in orange and**
 262 **HadISST in green.** The unshaded period corresponds to 2014–2015, during which the Blob occurred.

263

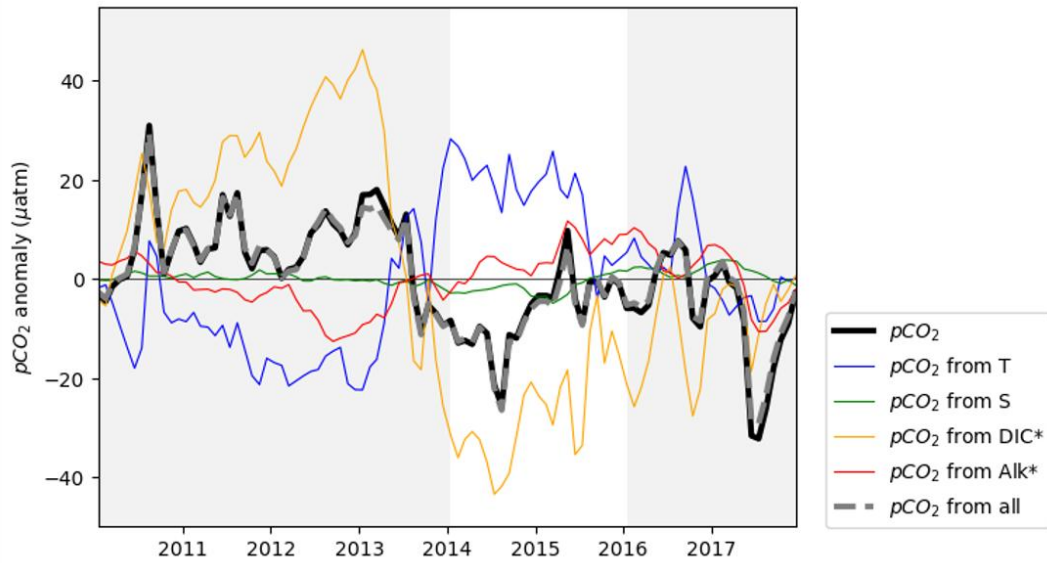
264 ~~DA~~Although direct observational constraints for evaluating the modeled carbonate system were limited for this region, we
 265 compared the model DIC and TALK outputs to with DIC and TALK fields provided by CMEMS-FFNN (Chau et al., 2024), one
 266 of the SeaFlux products. It should be noted that, in CMEMS-FFNN, TALK was estimated using a locally interpolated alkalinity
 267 regression (Carter et al., 2016, 2018) based on SST, SSS, nitrate, and silicate, while DIC was reconstructed from oceanic
 268 pCO₂ and TALK. In the mean spatial distributions for 2010–2017 (Fig. S1), both DIC and TALK were generally higher in the
 269 model than in CMEMS-FFNN, particularly in the northwestern part of the model domain. However, these differences were

270 relatively small in the central GOA near OSP, and this spatial feature was consistent with biases seen in other variables, such
271 as nutrients and oceanic pCO₂.

272
273 At OSP, the model showed higher DIC concentrations than CMEMS-FFNN (+11.4 μmol kg⁻¹ during the Blob), particularly
274 in autumn when CMEMS-FFNN had indicated relatively low DIC values (Fig. S2). Nevertheless, the temporal variability
275 agrees well between the two products, although the model had exhibited a smaller seasonal amplitude. For TALK, the model
276 generally showed higher concentrations than CMEMS-FFNN (+7.55 μmol kg⁻¹ during the Blob), except briefly in 2015. For
277 both variables, the model reproduced the decrease in concentrations during the Blob that was also seen in CMEMS-FFNN,
278 indicating consistent temporal changes before, during, and after the Blob between the two products. Compared with the in-situ
279 observations (Franco et al., 2021), both the model and CMEMS-FFNN showed statistically significant differences in TALK.
280 For DIC, a statistically significant difference was found in the model, whereas no significant difference was detected in
281 CMEMS-FFNN. However, a more rigorous assessment of model fidelity for DIC and TALK would require additional
282 observational data.

283 **3.3 Decomposition of pCO₂ variability**

284 Oceanic pCO₂ fluctuations can be explained by four components: temperature, salinity, DIC* and ALK* (Eq. 1). The
285 decomposition was applied to the variability of oceanic pCO₂ at OSP, revealing that the warming-induced increase d
286 in oceanic pCO₂ was fully compensated by the opposing changes in DIC during the Blob. First, the detrended and
287 deseasonalized oceanic pCO₂ time series was calculated and averaged within the 24 km radius of OSP. Similarly, the time
288 series of ~~the~~ SST, SSS, DIC*, and ALK* ~~were~~ calculated and Eq. (1) was applied to estimate the oceanic pCO₂ anomalies
289 (Fig. ~~65~~4). The oceanic pCO₂ changes from SSS and ALK* ~~were~~ small, while SST and DIC* changes ~~were~~ the main
290 drivers of the oceanic pCO₂ changes. The mooring observations showed d that oceanic pCO₂ increase ds due to SST changes
291 during the Blob by about +20 μatm, but decreasing oceanic pCO₂ from DIC* changes were even larger, around -30
292 μatm. Therefore, the net changes in oceanic pCO₂ caused by SST and DIC are compensated, and the net oceanic
293 pCO₂ change of around -10 μatm was primarily driven by the DIC, explaining the oceanic pCO₂ decreases during the
294 Blob.



295

296

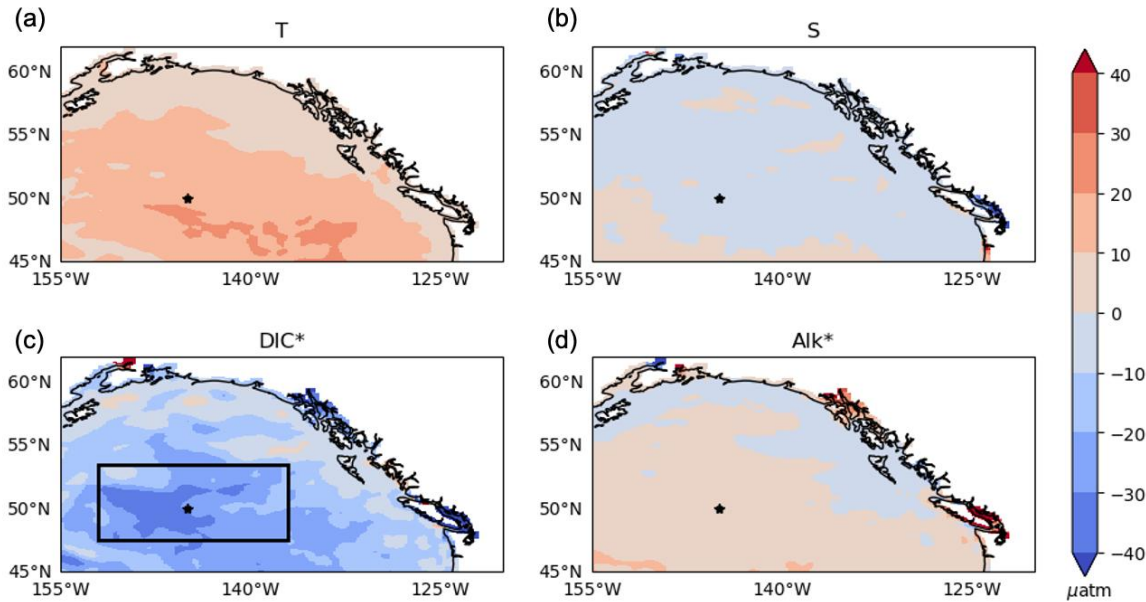
297

298

299

300

Figure 654: Time series of the contributions to oceanic $p\text{CO}_2$ anomaly referenced to 2010–2017 from SST (blue), SSS (green), DIC^* (yellow), ALK^* (red), and the combined effect of all variables (grey dashed) at OSP. The black line is the oceanic $p\text{CO}_2$ directly output from the model. All variables are detrended and deseasonalized. The unshaded period corresponds to 2014–2015, during which the Blob occurred. The grey dash line is the sum of individual components that closely matches the total $p\text{CO}_2$, supporting the linearity of Eq (1).



301

302

303

304

Figure 765: Spatial patterns of the contributions to oceanic $p\text{CO}_2$ from (a) SST, (b) SSS, (c) DIC^* , and (d) ALK^* during 2014–2015. Blue shows CO_2 uptake, and red shows CO_2 outgassing. The star in each panel marks the location of OSP. The black box (47.5–53.5°N, 208–223°E) in (c) indicates the central GOA open-ocean area used for the budget analysis shown in Figs. 76 and 87.

305 The decrease in DIC during the Blob happened ~~eds~~ not only at OSP but throughout the whole central GOA. Figure ~~765~~ showed ~~eds~~
306 the spatial distributions of the oceanic pCO₂ changes calculated from the model outputs of each variable, same as in Fig. ~~654~~
307 during the Blob. The characteristic described above, namely, the mutual compensation between the SST and DIC, also held ~~eds~~
308 in the entire region. These two factors counteract ~~ed~~ each other, resulting in a relatively small decrease in oceanic pCO₂ due to
309 the larger decrease in DIC. The magnitude of the oceanic pCO₂ declined ~~d~~ peaks in the central GOA around the location of OSP.

310 **3.4 Simulated DIC mass balance**

311 To investigate the factors causing the significant decrease in DIC during the Blob, the surface ocean DIC mass balance ~~was~~
312 examined by the diagnosis of the DIC tendency terms. In the simplest form, the DIC mass balance ~~was~~ explained by three
313 components: physical transport, biological activity, and air–sea gas exchanges.

314

$$315 \quad \frac{dC}{dt} = (\text{transport}) + (\text{biological activity}) + (\text{air} - \text{sea gas transfer}) \#(2)$$

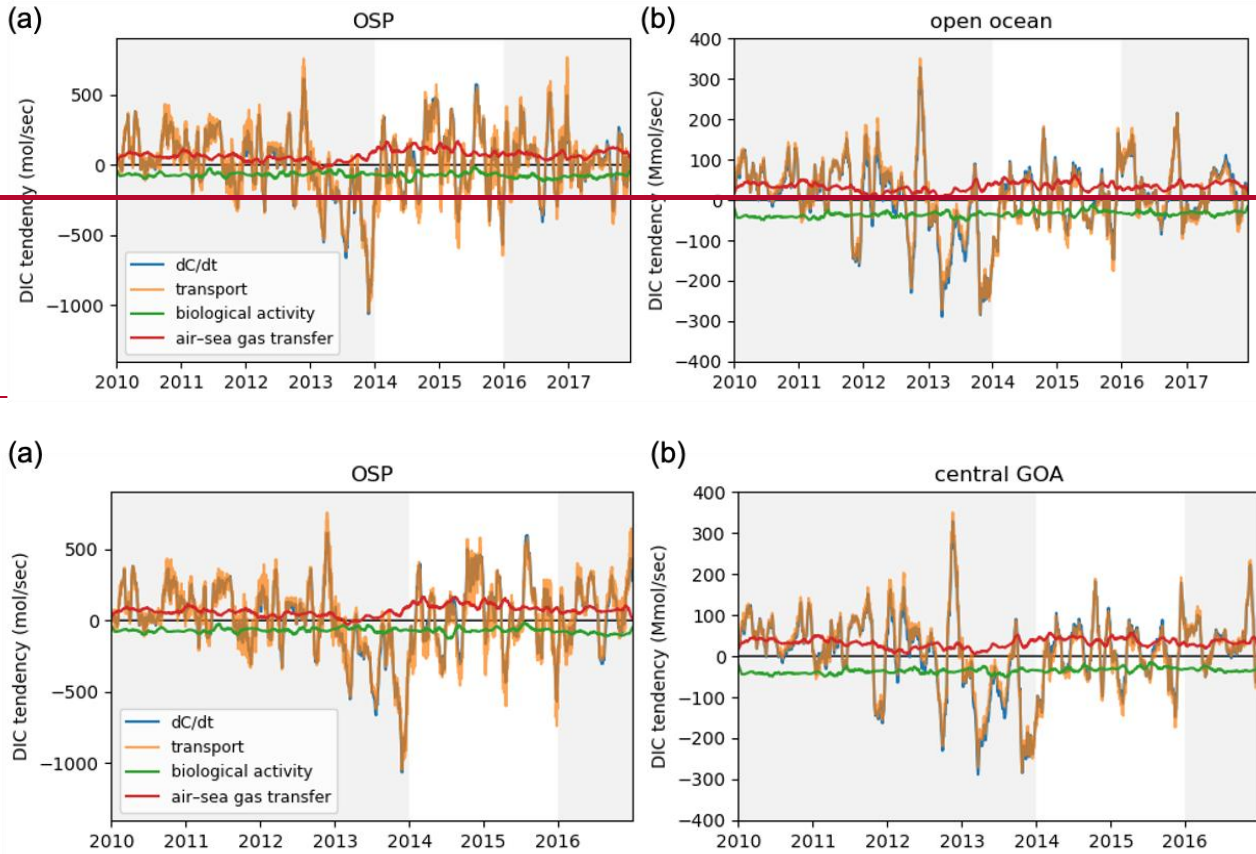
316

317 On the right-hand side of Eq. 2, the transport term include ~~eds~~ resolved advective transport convergence and parameterized
318 mixing terms. Zonal, meridional and vertical advection of DIC, parameterized mixing, as well as the total transport
319 convergence ~~were~~ calculated online and recorded as daily means. Biological activity include ~~eds~~ the net effects of
320 photosynthetic carbon fixation, phytoplankton mortality, remineralization of dissolved and particulate organic matter, and the
321 production and dissolution of calcium carbonates. These carbon tendency terms ($\frac{dC}{dt}$) ~~were~~ calculated for each timesteps and
322 ~~were~~ recorded as daily averages. The tendency terms calculated at OSP ~~were~~ integrated over the 24-km radius centred
323 at OSP. ~~To put OSP into context within the larger region (central GOA), rates were calculated For the larger central GOA open-~~
324 ~~ocean surrounding the OSP, they are calculated~~ within 47.5–53.5°N, 208–223°E, ~~shown~~ indicated with ~~by~~ ~~at~~ the black box in Fig.
325 ~~765c~~. In both cases, the tendencies ~~were~~ integrated from the surface to 177.5 m, with units of molC_s⁻¹. This depth range
326 ~~was~~ greater than the maximum mixed layer depth diagnosed in our simulation and thus guarantees that vertical integration
327 contain ~~eds~~ the entire mixed layer regardless of seasonal variability.

328

329 Figure ~~876~~ show ~~eds~~ the time series of each carbon tendency component at OSP (within 24 km radius) and in the ~~central~~
330 ~~GOA open-ocean~~ (box in Fig ~~65c~~), after removing the linear trend and mean seasonal cycle and applying a 30-day moving
331 window average. First, the sum of these three tendency components (Eq. 2) exactly match ~~eds~~ the DIC tendency (i.e. left-hand
332 side of Eq. 2). The variability of DIC ~~was~~ almost completely explained by the transport term throughout the entire period,
333 while the effects of the other two components ~~were~~ relatively minor. At OSP, an extremely negative anomaly in DIC
334 transport convergence rapidly developed in the winter of 2013, coinciding with the onset of the Blob. This anomaly ~~was~~
335 unprecedented compared to other periods. In the ~~central GOA open-ocean~~, a negative DIC transport anomaly appeared slightly

336 earlier, in early 2013, and, as at OSP, intensified again in the winter of 2013. These anomalies led to a pronounced DIC
 337 decrease at the onset of the Blob, driven by changes in physical transport processes.



338

339

340 **Figure 876:** Time series of vertically integrated DIC tendencies from the surface to 177.5 m at (a) OSP and (b) the **central GOA open**
 341 **ocean** which is defined in Fig. 765c. The time derivative of DIC is shown in blue; changes in DIC due to transport are shown in
 342 orange, due to biological activity in green, and due to air–sea gas transfer in red. All variables are detrended, deseasonalized, and
 343 smoothed using a 30-day moving average. The unshaded period corresponds to 2014–2015, during which the Blob occurred.

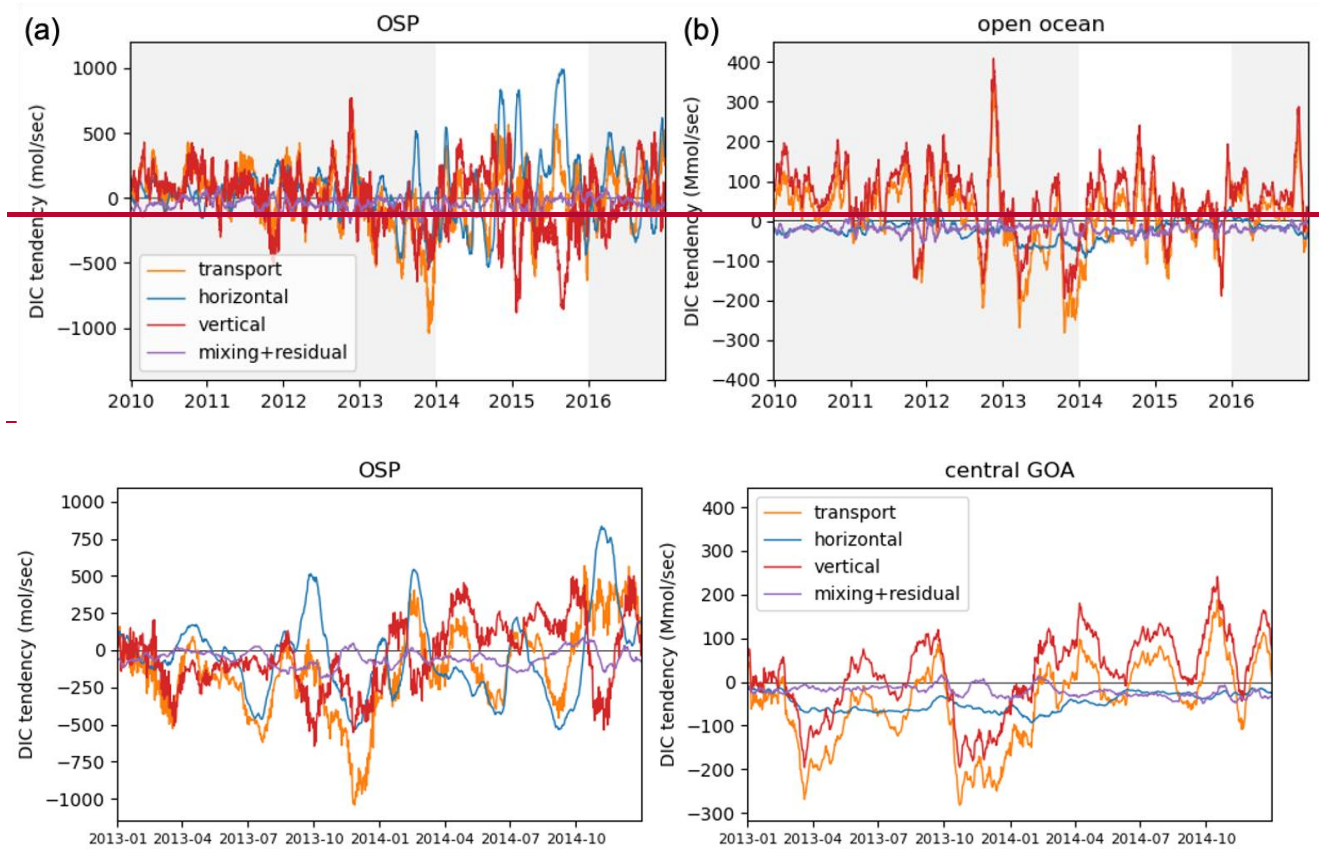
344

345 Among the physical processes responsible for the DIC reduction during the Blob, the vertical transport dominated over the
 346 large-scale domain, whereas locally the effects of the horizontal transport were comparable to those of the vertical transport.
 347 To better understand the transport-driven DIC changes, the transport term can be decomposed into individual components
 348 (horizontal and vertical advection) and the parameterized turbulent mixing terms. The background physical transport of DIC
 349 in the GOA was governed by both vertical and horizontal advection processes. Upwelling supplies DIC-enriched subsurface
 350 waters to the surface, while the prevailing westerlies drove a southward Ekman transport of DIC-rich surface waters from the
 351 northern part of the domain, where surface DIC concentrations were higher, to the southern part of the domain (Fig.
 352 S1a). Among the physical processes responsible for the DIC reduction during the Blob, the vertical transport dominated over

353 ~~the large-scale domain, whereas locally the effects of the horizontal transport are comparable to those of the vertical transport.~~
354 Figure 987 shows ~~eds~~ the time series of each advective component of DIC tendency at OSP and in the ~~central GOA open ocean.~~
355 In the ~~central GOA open ocean~~, the transport-driven DIC changes ~~were~~ primarily controlled by the vertical transport. This
356 ~~was~~ because the small-scale horizontal transport within the computational domain ~~was~~ averaged out, and the transport
357 across the domain boundaries ~~can~~ only play secondary roles in the regional DIC budget. Focusing on the DIC decrease in
358 the winter of 2013, a pronounced ~~DIC~~ reduction associated with ~~decreased~~ the vertical transport ~~was~~ evident, indicating
359 suppressed upward transport of DIC-rich waters from the ocean interior to the surface layer due to enhanced stratification
360 caused by elevated water temperatures. ~~In addition, the decrease in DIC attributable to the horizontal transport is also~~
361 ~~substantial compared to other years.~~

362
363 At OSP, the effect of the horizontal transport ~~was~~ more important locally relative to the larger domain in the ~~central GOA open~~
364 ~~ocean~~. Changes in DIC reflected ~~ed~~ the combined contributions of the vertical and horizontal transport, and their relative
365 contributions ~~were~~ quantified. In the winter of 2013, the net contribution of the horizontal
366 transport accounted for approximately half of the total DIC decrease ($-531.0 \text{ molCs}^{-1}$),
367 while the remaining half was attributable to a reduction in the vertical transport (-533.7
368 molCs^{-1}). ~~This DIC decrease associated with horizontal transport resulted from strengthened south-easterly currents in the~~
369 ~~winter of 2013. As shown in Fig. S3, anomalous south-easterly currents intensified from autumn to winter 2013, reducing the~~
370 ~~southward transport of DIC-rich surface waters that was typically supplied by Ekman transport from the north. However, as~~
371 ~~noted above, such south-easterly flow anomalies were not clearly evident over the entire model domain. Figure S3 also shows~~
372 ~~a clear shift toward negative DIC anomalies from 2013 to 2014. This DIC decrease associated with the horizontal transport~~
373 ~~resulted from strengthened south-easterly currents in the winter of 2013, which advected low-DIC water masses northward,~~
374 ~~leading to negative DIC anomalies in 2014 (Figs. S1 and S2).~~ Consequently, the local DIC reduction at OSP during the Blob
375 ~~was~~ driven by two mechanisms: anomalous south-to-north transport of low-DIC waters and suppressed upward transport of
376 DIC-rich subsurface waters. These transport anomalies ~~were~~ consistent with the reduced Ekman transport associated with
377 the weakened Aleutian Low that generated the anomalously high sea level pressure and SST (Bond et al., 2015; Hartmann et
378 al., 2015).

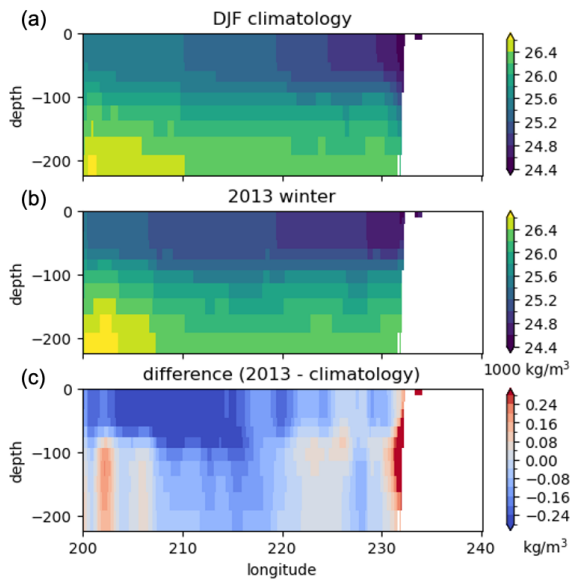
379



382 **Figure 987:** Time series of vertically integrated DIC tendencies from the surface to 177.5 m at (a) OSP and (b) the **central GOA open**
 383 **ocean**, which is defined in Fig. 765c, for each transport component: horizontal advection (blue), vertical advection (red), and the
 384 **mixing and residual term** (purple), calculated as the remainder after subtracting the advective components from the total transport
 385 **(orange)**. All variables are detrended, deseasonalized, and smoothed using a 30-day moving average. The unshaded period
 386 **corresponds to 2014–2015**, during which the Blob occurred.

387 **3.5 Drivers of the simulated weakening of physical transport**

388 The reduction in vertical DIC transport in the central GOA was driven by two key mechanisms: enhanced stratification
 389 associated with SST warming and weakened Ekman pumping caused by reduced wind-driven circulation. Compared with the
 390 DJF climatology, potential density in the winter 2013 exhibited substantially lower between 160°W and 140°W (Fig. 109),
 391 indicating strengthened stratification that suppressed the upward transport of DIC-rich subsurface waters and reduced the DIC
 392 supply to the surface.

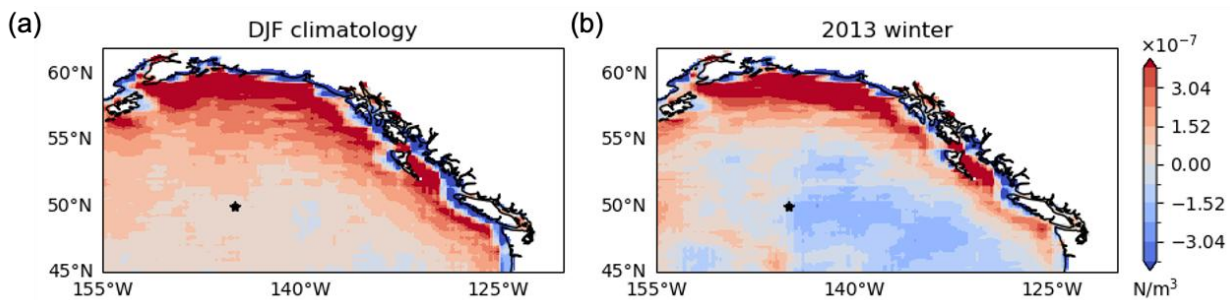


393

394 **Figure 109: Vertical cross-sections of potential density along 50.5°N for (a) the DJF-mean climatology over 2010–2017, (b) 2013, and**
 395 **(c) their difference (2013 minus climatology).**

396

397 In addition, although the GOA was typically characterized by Ekman upwelling, the period immediately preceding the onset
 398 of the Blob was marked by weakened wind stress curl and Ekman downwelling (Fig. 110), further suppressing the vertical
 399 DIC supply. These potential density and wind stress curl changes were fully consistent with both the marine heatwave itself
 400 and the weakening of the Aleutian Low that initiated the Blob. Together, these early-stage changes reduced surface DIC and
 401 exerted a substantial influence on oceanic pCO₂ throughout the Blob period. This highlights the critical role of early physical
 402 forcing in shaping the prolonged carbon cycle response during the Blob.

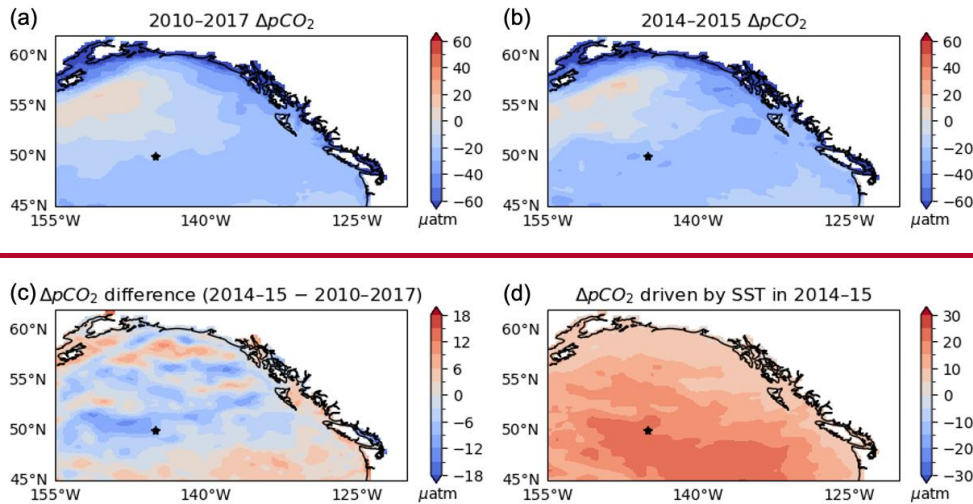


403

404 **Figure 110: Spatial patterns of wind stress curl ($\text{curl}\tau$) for (a) the DJF-mean climatology over 2010–2017 and (b) 2013.**
 405 **Positive values indicate cyclonic flow associated with Ekman upwelling. The star in each panel marks the location of OSP.**

406 4 Discussion

407 Consistent with the observations, the model indicates that increasing SST cannot account for the changes in oceanic pCO₂
408 under the Blob, not only at OSP but across the entire GOA (Fig. 118). Compared to the observations (Fig. 21), ΔpCO₂ driven
409 by SST under the Blob in the model is approximately 5 μatm higher around OSP. Despite the moderate overestimation in
410 thermal driven pCO₂ anomaly, the modeled ΔpCO₂ shows a significant decrease across the central GOA, consistent with the
411 SeaFlux dataset and the mooring observation at OSP. This consistency is underscoring the robustness of the modeled response.
412 Throughout the region, the effect of warming induced increase in the oceanic pCO₂ is offset by the oceanic pCO₂ reduction
413 driven by decreased DIC, which is consistent with the previous work by Kohlman et al. (2024).



414
415 **Figure 118: Same as Fig. 21 but for the model results.**

416
417 Both the model and the SeaFlux product showed enhanced oceanic CO₂ uptake during the Blob period. This increase was
418 primarily driven by changes in surface ocean pCO₂. Here, CO₂ flux was treated as a complementary diagnostic of the integrated
419 air-sea CO₂ response to the Blob, given its nonlinear dependence on wind speed, temperature, and ΔpCO₂. The spatial
420 distribution of the CO₂ flux indicated net oceanic CO₂ uptake over most of the GOA domain, while enhanced outgassing
421 (ocean to atmosphere), which was not evident in SeaFlux ensemble mean, was simulated in the northwestern region relative
422 to the SeaFlux product (Fig. S4), consistent with the elevated oceanic pCO₂ in this area (Figs. 2 and 38). This positive bias in
423 the northwestern GOA was also reflected in other variables, such as nutrients.

424
425 In the area-integrated CO₂ flux time series for the central GOA (Fig. S5), the model exhibited weaker uptake than the SeaFlux
426 ensemble mean during all periods, with values of -8.2 Tg yr⁻¹ versus -10.9 Tg yr⁻¹ before the Blob (2010-2013), (-13.4 Tg
427 yr⁻¹ in the model versus -19.0 Tg yr⁻¹ in the SeaFlux ensemble mean during the Blob (2014-2015), and -12.9 Tg yr⁻¹ versus
428 -14.8 Tg yr⁻¹ after the Blob (2017), respectively (the model versus the SeaFlux ensemble mean) period). Given that both

429 ~~products use JRA55 winds and that differences in CO₂ solubility are negligible, this discrepancy likely arises from differences~~
430 ~~in $\Delta p\text{CO}_2$ and/or the gas transfer coefficient. Notably, the modeled $\Delta p\text{CO}_2$ flux was smaller than the SeaFlux ensemble mean,~~
431 ~~particularly in 2015 (Fig. S5). However, both the model and the SeaFlux ensemble showed overall good agreement with the~~
432 ~~mooring observations (Fig. 54), although the degree of agreement varies by year. Therefore, the weaker modeled CO₂ uptake~~
433 ~~does not necessarily imply reduced model fidelity.~~

434
435 Our results showed that the reduction in DIC during the Blob was primarily driven by physical processes such as Ekman
436 transport and vertical entrainment. Beyond the oceanic pCO₂ changes, numerous biological impacts of MHWs have also been
437 reported. These include observed declines in annual net community production (Yang et al., 2018), reductions and taxonomic
438 shifts in phytoplankton biomass, transitions in plankton communities from larger to smaller taxa (Du and Peterson, 2018; Peña
439 et al., 2018; Baetten et al., 2022). Whether ecosystem impacts can return to pre-MHW conditions remains uncertain (Suryan
440 et al., 2021). The magnitude and nature of these biological responses vary greatly among regions, and a key factor is whether
441 the area is primarily limited by nitrate or iron to the biological production (Peña et al., 2018; Hayashida et al., 2020; Wyatt et
442 al., 2022). Because the GOA is an iron-limited region, it is likely less sensitive to MHW-induced macro-nutrient reductions
443 than regions farther south in the subtropics and the transition zone (30–45°N, Wyatt et al., 2022). Nevertheless, model-based
444 analyses will be essential for assessing long-term and basin-scale impacts. The biogeochemical model used in this study is
445 relatively simple, and it does not explicitly represent shifts in plankton community composition. Revisiting this problem with
446 a more sophisticated ecosystem model would be warranted to assess such ecological changes and determine their duration and
447 magnitude.

448
449 ~~Compared~~Comparing to the study conducted over broader spatial domains (Mignot et al., 2022), our results revealed a distinct
450 response of oceanic pCO₂ to MHWs in the GOA. This highlights the importance of investigating the impacts of MHWs on
451 oceanic pCO₂ in other regions as well. For instance, persistent positive SST anomalies have also been reported in the western
452 North Pacific, particularly in the Oyashio region (40–43°N and 143–147°E, Miyama et al., 2021), which is one of the major
453 carbon uptake areas in the basin. However, it remains unclear how oceanic pCO₂ in this region responded to such anomalies.
454 It is important to expand the model domain to a broader area including the western North Pacific.

455
456 Abnormally high ocean temperatures like the Blob have been increasing in both frequency and duration (Frölicher et al., 2018;
457 Oliver et al., 2018). The North Pacific experienced anomalously high SSTs in other years such as 2019 (Amaya et al., 2020)
458 and 2023 (Dong et al., 2025). These MHWs exhibit even larger SST anomalies than the Blob and differ in several key
459 characteristics, such as the timing of the peak warming (Amaya et al., 2020). Consequently, their impacts on oceanic pCO₂,
460 carbon cycling, and marine ecosystems may differ from those during the Blob. Indeed, the 2023 MHW showed a markedly
461 different behaviour on the global scale, with an approximately 10% reduction in oceanic CO₂ uptake, substantially larger than
462 in previous events (Müller et al., 2025). These contrasts call for event-specific investigations of individual MHWs. In this

463 context, a similar analysis of the 2005 warm anomaly event in the GOA showed qualitatively comparable results to the Blob,
464 in that the DIC decrease and associated reduction in oceanic pCO₂ were primarily controlled by changes in vertical transport.
465 Although not shown, these results suggest that the proposed mechanism may operate under certain warm anomaly conditions
466 in the GOA. However, its applicability is not necessarily universal and may depend on the characteristics and intensity of
467 individual events, particularly for recent stronger MHWs. In this context, a similar analysis of the 2005 warm anomaly event
468 in the GOA produced comparable results to the Blob, showing that the DIC decrease leading to reduced oceanic pCO₂ was
469 also primarily controlled by changes in vertical transport. Although these results are not shown, they support the robustness of
470 the proposed mechanism across multiple warm anomaly events in the GOA. These results suggest that the proposed mechanism
471 might be relevant to some warm anomaly events in the GOA, but its applicability appeared to depend on the characteristics of
472 individual events, and might not hold under increasingly intense recent MHW conditions.

473

474 The model employed in this study was integrated only through 2017 due to the availability of the open boundary conditions.
475 Future work should extend the integration period, for instance by applying alternative boundary conditions, to assess the
476 impacts of the 2019 and 2023 MHWs on oceanic pCO₂.

477 **5 Conclusions**

478 From the winter of 2013 to 2015, the eastern North Pacific experienced an anomalously high in SST. Contrary to expectations
479 based on the reduced CO₂ solubility under warming, oceanic pCO₂ did not rise. Instead, it decreased across the entire region,
480 with a particularly large decrease in the open ocean (Figs. 24 and 43). To investigate why oceanic pCO₂ broadly decreased
481 during the Blob, the simulation results from the regional ocean circulation and biogeochemistry model were analyzed. The
482 model represents the oceanic pCO₂ remarkably well compared to the observations (Figs. 32 and 43). The decomposition of the
483 oceanic pCO₂ anomalies into four components shows that the variability in the oceanic pCO₂ is primarily dominated by changes
484 in SST and DIC. Furthermore, the effects of these two factors generally compensate for one another. During the Blob, the
485 reduction in oceanic pCO₂ due to a decrease in DIC was stronger in magnitude than the warming-induced increase (Figs. 54
486 and 65). The pronounced reduction in DIC under the Blob is attributable not to biological processes, but rather to the anomalous
487 physical transport (Fig. 76). In particular, reduced vertical DIC transport in the central GOA, driven by enhanced stratification
488 and weakened Ekman pumping, was the primary mechanism (Figs. 8–10). Consequently, these changes in the vertical
489 circulation decreased the surface DIC concentrations, leading to a subsequent decline in the oceanic pCO₂ during the Blob.
490 Typically, DIC-rich water masses are transported from north to south by the wind-driven Ekman transport. However, during
491 the Blob, DIC-poor water masses are advected from south to north (Fig. 7). Furthermore, increased stratification reduced the
492 upward entrainment of subsurface DIC-rich waters. Consequently, these changes in the horizontal and vertical circulation field
493 decreased the surface DIC concentrations, driving a subsequent decline in the oceanic pCO₂.

494

495 **Data availability**

496 The monthly and daily model output data used in this study are archived on Zenodo (doi: 10.5281/zenodo.18462325). The
497 data will be made publicly available upon publication of the associated article.

498 **Author contribution**

499 TI conceptualized and designed the model, and YA performed the simulations and analyses. AT contributed observational
500 comparison and interpretation. YA wrote the original draft of the manuscript. TI, AT, CR, and JM reviewed and edited the
501 manuscript and contributed to scientific discussion. All authors approved the final version of the manuscript.

502 **Competing interests**

503 The authors declare that they have no conflict of interest.

504 **Acknowledgements**

505 This study is supported by the US National Science Foundation (OCE-2241931). The source code for MITgcm is available in
506 the public domain (Campin et al., 2025)

507 **References**

- 508 Amaya, D. J., Miller, A. J., Xie, S.-P., and Kosaka, Y.: Physical drivers of the summer 2019 North Pacific marine heatwave,
509 *Nat. Commun.*, 11, 1903, doi:10.1038/s41467-41020-15820-w, 2020.
- 510 Barbeaux, S. J., Holsman, K., and Zador, S.: Marine heatwave stress test of ecosystem-based fisheries management in the Gulf
511 of Alaska Pacific cod fishery, *Front. Mar. Sci.*, 7, 703, doi:10.3389/fmars.2020.00703, 2020.
- 512 Batten, S. D., Ostle, C., Hélaouët, P., and Walne, A. W.: Responses of Gulf of Alaska Plankton Communities to a Marine Heat
513 Wave, *Deep Sea Research Part II: Topical Studies in Oceanography*, 195, 105002, doi:10.1016/j.dsr2.2021.105002, 2022.
- 514 Bond, N. A., Cronin, M. F., Freeland, H., and Mantua, N.: Causes and impacts of the 2014 warm anomaly in the NE Pacific,
515 *Geophys. Res. Lett.*, 42, 3414–3420, doi:10.1002/2015gl063306, 2015.
- 516 Burger, F. A., Terhaar, J., and Frölicher, T. L.: Compound marine heatwaves and ocean acidity extremes, *Nat. Commun.*, 13,
517 4722, doi:10.1038/s41467-022-32120-7, 2022.
- 518 Campin, J.-M., Heimbach, P., Losch, M., Forget, G., edhill3, Adcroft, A., amolod, Menemenlis, D., dfer22, Jahn, O., Hill, C.,
519 Scott, J., dngoldberg, stephdut, Mazloff, M., Fox-Kemper, B., antnguyen13, Doddridge, E., Fenty, I., Bates, M., Wang, O.,
520 Smith, T., AndrewEichmann, N., mitllheisey, Lauderdale, J., Martin, T., Abernathy, R., samarkhathiwala, hongandyan, and
521 Escobar, I.: MITgcm/MITgcm: checkpoint69e (Version checkpoint69e), Zenodo, doi:10.5281/zenodo.15320163, 2025.

- 522 [Carter, B. R., Williams, N. L., Gray, A. R., and Feely, R. A.: Locally interpolated alkalinity regression for global alkalinity](#)
523 [estimation, *Limnol. Oceanogr.-Meth.*, 14, 268–277, doi:1002/lom3.10087, 2016.](#)
- 524 [Carter, B. R., Feely, R. A., Williams, N. L., Dickson, A. G., Fong, M. B., and Takeshita, Y.: Updated methods for global](#)
525 [locally interpolated estimation of alkalinity, pH, and nitrate, *Limnol. Oceanogr.-Meth.*, 16, 119–131, doi:10.1002/lom3.10232,](#)
526 [2018.](#)
- 527 Carton, J. A., and Giese, B. S.: A Reanalysis of Ocean Climate Using Simple Ocean Data Assimilation (SODA), *Mon. Weather*
528 *Rev.*, 136, 2999–3017, doi:10.1175/2007MWR1978.1, 2008.
- 529 Carton, J. A., Chepurin, G. A., and Chen, L.: SODA3: A new ocean climate reanalysis, *J. Clim.*, 31, 6967–6983,
530 doi:10.1175/JCLI-D-17-0149.1, 2018.
- 531 Cavole, L., Demko, A., Diner, R., Giddings, A., Koester, I., Pagniello, C., Paulsen, M.-L., Ramírez-Valdez, A., Schwenck, S.,
532 Zill, M., and Franks, P.: Biological Impacts of the 2013–2015 Warm-Water Anomaly in the Northeast Pacific: Winners, Losers,
533 and the Future, *Oceanography*, 29, 273–285, doi:10.5670/oceanog.2016.32, 2016.
- 534 [Chau, T.-T.-T., Gehlen, M., Metzl, N., and Chevallier, F.: CMEMS-LSCE: a global, 0.25°, monthly reconstruction of the](#)
535 [surface ocean carbonate system, *Earth Syst. Sci. Data*, 16, 121–160, doi:10.5194/essd-16-121-2024, 2024.](#)
- 536 Coyle, K. O., Cheng, W., Hinckley, S. L., Lessard, E. J., Whitlege, T., Hermann, A. J., and Hedstrom, K.: Model and field
537 observations of effects of circulation on the timing and magnitude of nitrate utilization and production on the northern Gulf of
538 Alaska shelf, *Prog. Oceanogr.*, 103, 16–41, doi:10.1016/j.pocean.2012.03.002, 2012.
- 539 Cronin, M. F., Pelland, N. A., Emerson, S. R., and Crawford, W. R.: Estimating diffusivity from the mixed layer heat and salt
540 balances in the North Pacific, *J. Geophys. Res.-Oceans*, 120, 7346–7362, doi:10.1002/2015jc011010, 2015.
- 541 Di Lorenzo, E., and Mantua, N.: Multi-year persistence of the 2014/15 North Pacific marine heatwave. *Nature Climate Change*,
542 6 (11), 1042–1047, doi:10.1038/nclimate3082, 2016.
- 543 Dong, T., Zeng, Z., Pan, M., Wang, D., Chen, Y., Liang, L., Yang, S., Jin, Y., Luo, S., Liang, S., Huang, X., Zhao, D., Ziegler,
544 A. D., Chen, D., Li, L. Z. X., Zhou, T., and Zhang, D.: Record-breaking 2023 marine heatwaves, *Science*, 389, 6758, pp. 369–
545 374, doi: 10.1126/science.adr0910, 2025.
- 546 Du, X., and Peterson, W. T.: Phytoplankton community structure in 2011–2013 compared to the extratropical warming event
547 of 2014–2015, *Geophys. Res. Lett.*, 45, 1534–1540, doi:10.1002/2017GL076199, 2018.
- 548 Duke, P. J., Hamme, R. C., Ianson, D., Landschützer, P., Ahmed, M. M. M., Swart, N. C., and Covert, P. A.: Estimating marine
549 carbon uptake in the northeast Pacific using a neural network approach, *Biogeosciences*, 20, 3919–3941, doi:10.5194/bg-20-
550 3919-2023, 2023.
- 551 Dunne, J. P., Bociu, I., Bronselaer, B., Guo, H., John, J. G., Krasting, J. P., Stock, C. A., Winton, M., and Zadeh, N.: Simple
552 Global Ocean Biogeochemistry with Light, Iron, Nutrients and Gas version 2 (BLINGv2): Model description and simulation
553 characteristics in GFDL's CM4.0, *J. Adv. Model. Earth Sy.*, 12, e2019MS002008, doi:10.1029/2019MS002008, 2020.
- 554 Emerson, S., Sabine, C., Cronin, M. F., Feely, R., Cullison Gray, S. E., and DeGrandpre, M.: Quantifying the flux of CaCO₃
555 and organic carbon from the surface ocean using in situ measurements of O₂, N₂, pCO₂, and pH, *Global Biogeochem. Cy.*,
556 25, GB3008, doi:10.1029/2010GB003924, 2011.

557 Fay, A. R., Gregor, L., Landschützer, P., McKinley, G. A., Gruber, N., Gehlen, M., Iida, Y., Laruelle, G. G., Rödenbeck, C.,
558 Roobaert, A., and Zeng, J.: SeaFlux: harmonization of air–sea CO₂ fluxes from surface pCO₂ data products using a
559 standardized approach, *Earth Syst. Sci. Data*, 13, 4693–4710, doi:10.5194/essd-13-4693-2021, 2021.

560 [Franco, A. C., Ianson, D., Ross, T., Hamme, R. C., Monahan, A. H., Christian, J. R., Davelaar, M., Johnson, W. K., Miller, L.](#)
561 [A., Robert, M., and Tortell, P. D.: Anthropogenic and climatic contributions to observed carbon system trends in the northeast](#)
562 [Pacific, *Global Biogeochem. Cy.*, 35, doi:10.1029/2020GB006829, 2021.](#)

563 [Friedlingstein, P., O'Sullivan, M., Jones, M. W., Andrew, R. M., Gregor, L., Hauck, J., Le Quéré, C., Luijkx, I. T., Olsen, A.,](#)
564 [Peters, G. P., Peters, W., Pongratz, J., Schwingshackl, C., Sitch, S., Canadell, J. G., Ciais, P., Jackson, R. B., Alin, S. R.,](#)
565 [Alkama, R., Arneeth, A., Arora, V. K., Bates, N. R., Becker, M., Bellouin, N., Bittig, H. C., Bopp, L., Chevallier, F., Chini, L.](#)
566 [P., Cronin, M., Evans, W., Falk, S., Feely, R. A., Gasser, T., Gehlen, M., Gkritzalis, T., Gloege, L., Grassi, G., Gruber, N.,](#)
567 [Gürses, Ö., Harris, I., Hefner, M., Houghton, R. A., Hurtt, G. C., Iida, Y., Ilyina, T., Jain, A. K., Jersild, A., Kadono, K., Kato,](#)
568 [E., Kennedy, D., Klein Goldewijk, K., Knauer, J., Korsbakken, J. I., Landschützer, P., Lefèvre, N., Lindsay, K., Liu, J., Liu,](#)
569 [Z., Marland, G., Mayot, N., McGrath, M. J., Metzl, N., Monacci, N. M., Munro, D. R., Nakaoka, S.-I., Niwa, Y., O'Brien, K.,](#)
570 [Ono, T., Palmer, P. I., Pan, N., Pierrot, D., Pockock, K., Poulter, B., Resplandy, L., Robertson, E., Rödenbeck, C., Rodriguez,](#)
571 [C., Rosan, T. M., Schwinger, J., Séférian, R., Shutler, J. D., Skjelvan, I., Steinhoff, T., Sun, Q., Sutton, A. J., Sweeney, C.,](#)
572 [Takao, S., Tanhua, T., Tans, P. P., Tian, X., Tian, H., Tilbrook, B., Tsujino, H., Tubiello, F., van der Werf, G. R., Walker, A.](#)
573 [P., Wanninkhof, R., Whitehead, C., Willstrand Wranne, A., Wright, R., Yuan, W., Yue, C., Yue, X., Zaehle, S., Zeng, J., and](#)
574 [Zheng, B.: Global Carbon Budget 2022, *Earth Syst. Sci. Data*, 14, 4811–4900, doi: 10.5194/essd-14-4811-2022, 2022.](#)

575 Frölicher, T. L., Fischer, E. M., and Gruber, N.: Marine heatwaves under global warming, *Nature*, 560, 360–364,
576 doi:10.1038/s41586-018-0383-9, 2018.

577 Gruber, N., Boyd, P. W., Frölicher, T. L., and Vogt, M.: Biogeochemical extremes and compound events in the ocean, *Nature*,
578 600, 395–407, doi:10.1038/s41586-021-03981-7, 2021.

579 Hartmann, D. L.: Pacific sea surface temperature and the winter of 2014, *Geophys. Res. Lett.*, 42, 1894–1902,
580 doi:10.1002/2015GL063083, 2015.

581 Hauri, C., Schultz, C., Hedstrom, K., Danielson, S., Irving, B., Doney, S. C., Dussin, R., Curchitser, E. N., Hill, D. F., and
582 Stock, C. A.: A regional hindcast model simulating ecosystem dynamics, inorganic carbon chemistry, and ocean acidification
583 in the Gulf of Alaska, *Biogeosciences*, 17, 3837–3857, doi:10.5194/bg-17-3837-2020, 2020.

584 Hayashida, H., Matear, R. J., and Strutton, P. G.: Background nutrient concentration determines phytoplankton bloom response
585 to marine heatwaves, *Global Change Biol.*, 26, 4800–4811, doi:10.1111/gcb.15255, 2020.

586 Hinckley, S., Coyle, K. O., Gibson, G., Hermann, A. J., and Dobbins, E. L.: A biophysical NPZ model with iron for the Gulf
587 of Alaska: reproducing the differences between an oceanic HNLC ecosystem and a classical northern temperate shelf
588 ecosystem, *Deep-Sea Res. Pt. II*, 56, 2520–2536, doi:10.1016/j.dsr2.2009.03.003, 2009.

589 Hobday, A. J., Alexander, L. V., Perkins, S. E., Smale, D. A., Straub, S. C., Oliver, E. C., Benthuisen, J. A., Burrows, M. T.,
590 Donat, M. G., Feng, M., Holbrook, N. J., Moore, P. J., Scannell, H. A., Sen Gupta, A., and Wernberg, T.: A hierarchical
591 approach to defining marine heatwaves, *Prog. Oceanogr.*, 141, 227–238, doi:10.1016/j.pocean.2015.12.014, 2016.

592 [Huang, B., Liu, C., Banzon, V., Freeman, E., Graham, G., Hankins, B., Smith, T., and Zhang, H.-M.: Improvements of the](#)
593 [Daily Optimum Interpolation Sea Surface Temperature \(DOISST\) Version 2.1, J. Climate, 34, 2923–2939, doi:10.1175/JCLI-](#)
594 [D-20-0166.1, 2021.](#)

595 Humphreys, M. P., Lewis, E. R., Sharp, J. D., and Pierrot, D.: PyCO2SYS v1.8: marine carbonate system calculations in
596 Python, *Geosci. Model Dev.*, 15, 15–43, doi:10.5194/gmd-15-15-2022, 2022.

597 [Ito, T., Timmerman, A. H. V., Bjorklund, A., Stanley, S. I., Abe, Y., Reinhard, C. T., and Montoya, J.: Eddy-induced iron](#)
598 [transport sustains the biological productivity in the Gulf of Alaska. J. Geophys. Res.-Oceans, 131, e2025JC022996, doi:](#)
599 [10.1029/2025JC022996, 2026.](#)

600 ~~[Ito, T., Timmerman, H. V. A., Bjorklund, A., Stanley, S. I., Abe, Y., Reinhard, C. T., and Montoya, J.: Eddy induced iron](#)~~
601 ~~[transport sustains the biological productivity in the Gulf of Alaska. ESS Open Archive.,](#)~~
602 ~~[doi:10.22541/essoar.175080521.18150857/v1, June 24, 2025.](#)~~

603 Keeling, C. D., Piper, S. C., Bacastow, R. B., Wahlen, M., Whorf, T. P., Heimann, M., and Meijer, H. A.: Exchanges of
604 Atmospheric CO₂ and ¹³CO₂ with the Terrestrial Biosphere and Oceans from 1978 to 2000. I. Global Aspects, SIO
605 REFERENCE, p. 29, <https://escholarship.org/uc/item/09v319r9> (last access: 06 Oct 2025), 2001.

606 Keeling, C. D., Brix, H., and Gruber, N.: Seasonal and long-term dynamics of the upper ocean carbon cycle at Station ALOHA
607 near Hawaii, *Global Biogeochem. Cy.*, 18, GB4006, doi:10.1029/2004GB002227, 2004.

608 Kohlman, C., Cronin, M. F., Dziak, R., Mellinger, D. K., Sutton, A., Galbraith, M., Robert, M., Thomson, J., Zhang, D., and
609 Thompson, L.: The 2019 marine heatwave at ocean station papa: A multi-disciplinary assessment of ocean conditions and
610 impacts on marine ecosystems, *J. Geophys. Res.-Oceans*, 129(6), e2023JC020167, doi:10.1029/2023JC020167, 2024.

611 Large, W. G., McWilliams, J. C., and Doney, S. C.: Ocean vertical mixing: a review and a model with a nonlocal boundary
612 layer parameterization, *Rev. Geophys.*, 32, 363–403, doi:10.1029/94RG01872, 1994.

613 Lauvset, S. K., Lange, N., Tanhua, T., Bittig, H. C., Olsen, A., Kozyr, A., Alin, S., Álvarez, M., Azetsu-Scott, K., Barbero, L.,
614 Becker, S., Brown, P. J., Carter, B. R., da Cunha, L. C., Feely, R. A., Hoppema, M., Humphreys, M. P., Ishii, M., Jeansson,
615 E., Jiang, L.-Q., Jones, S. D., Lo Monaco, C., Murata, A., Müller, J. D., Pérez, F. F., Pfeil, B., Schirnick, C., Steinfeldt, R.,
616 Suzuki, T., Tilbrook, B., Ulfso, A., Velo, A., Woosley, R. J., and Key, R. M.: GLODAPv2.2022: the latest version of the
617 global interior ocean biogeochemical data product, *Earth Syst. Sci. Data*, 14, 5543–5572, doi:10.5194/essd-14-5543-2022,
618 2022.

619 Li, C., Burger, F. A., Raible, C. C., and Frölicher, T. L.: Observed Regional Impacts of Marine Heatwaves on Sea-Air CO₂
620 Exchange, *Geophys. Res. Lett.*, 51, e2024GL110379, doi:10.1029/2024GL110379, 2024a.

621 Li, C., Huang, J., Liu, X., Ding, L., He, Y., and Xie, Y.: The ocean losing its breath under the heatwaves, *Nat. Commun.*, 15,
622 6840, doi:10.1038/s41467-024-51323-8, 2024b.

623 Losch, M., Menemenlis, D., Campin, J.-M., Heimbach, P., and Hill, C.: On the formulation of sea-ice models. Part 1: Effects
624 of different solver implementations and parameterizations, *Ocean Model.*, 33, 129–144, doi:10.1016/j.ocemod.2009.12.008,
625 2010.

626 Manizza, M., Le Quéré, C., Watson, A. J., and Buitenhuis, E. T.: Bio-optical feedbacks among phytoplankton, upper ocean
627 physics and sea-ice in a global model, *Geophys. Res. Lett.*, 32, L05603, doi:10.1029/2004gl020778, 2005.

- 628 Marshall, J., Adcroft, A., Hill, C., Perelman, L., and Heisey, C.: A finite-volume, incompressible Navier Stokes model for
629 studies of the ocean on parallel computers, *J. Geophys. Res.-Oceans*, 102, 5753–5766, doi:10.1029/96JC02775, 1997a.
- 630 Marshall, J., Hill, C., Perelman, L., and Adcroft, A.: Hydrostatic, quasi-hydrostatic, and nonhydrostatic ocean modeling, *J.*
631 *Geophys. Res.-Oceans*, 102, 5733–5752, doi:10.1029/96JC02776, 1997b.
- 632 McKinley, G. A., Takahashi, T., Buitenhuis, E., Chai, F., Christian, J.R., Doney, S. C., Jiang, M. S., Lindsay, K., Moore, J.
633 K., Le Quéré, C., Lima, I., Murtugudde, R., Shi, L., and Wetzel, P.: North Pacific carbon cycle response to climate variability
634 on seasonal to decadal timescales, *J. Geophys. Res.*, 111, C07S06, doi:10.1029/2005JC003173, 2006.
- 635 Mignot, A., Schuckmann, K. V., Landschützer, P., Gasparin, F., Gennip, S. V., Perruche, C., Lamouroux, J., and Amm, T.:
636 Decrease in air-sea CO₂ fluxes caused by persistent marine heatwaves, *Nat. Commun.*, 13, 1–9, doi:10.1038/s41467-022-
637 31983-0, 2022.
- 638 Miyama, T., Minobe, S., and Goto, H.: Marine Heatwave of Sea Surface Temperature of the Oyashio Region in Summer in
639 2010–2016, *Front. Mar. Sci.*, 7:576240, doi:10.3389/fmars.2020.576240, 2021.
- 640 Mogen, S. C., Lovenduski, N. S., Dallmann, A. R., Gregor, L., Sutton, A. J., Bograd, S. J., Quiros, N. C., Di Lorenzo, E.,
641 Hazen, E. L., Jacox, M. G., Buil, M. P., and Yeager, S.: Ocean Biogeochemical Signatures of the North Pacific Blob, *Geophys.*
642 *Res. Lett.*, 49, e2021GL096938, doi:10.1029/2021GL096938, 2022.
- 643 Müller, J. D., Gruber, N., Schneuwly, A., Bakker, D. C. E., Gehlen, M., Gregor, L., Hauck, J., Landschützer, P., and McKinley,
644 G. A.: Unexpected decline in the ocean carbon sink under record-high sea surface temperatures in 2023. *Nat. Clim. Chang.* 15,
645 978–985, doi:10.1038/s41558-025-02380-4, 2025.
- 646 Oliver, E. C. J., Donat, M. G., Burrows, M. T., Moore, P. J., Smale, D. A., Alexander, L. V., Benthuisen, J. A., Feng, M., Sen
647 Gupta, A., Hobday, A. J., Holbrook, N. J., Perkins-Kirkpatrick, S. E., Scannell, H. A., Straub, S. C., and Wernberg, T.: Longer
648 and more frequent marine heatwaves over the past century, *Nat. Commun.*, 9, 1324, doi:10.1038/s41467-018-03732-9, 2018.
- 649 Peña, M. A., Nemcek, N., and Robert, M.: Phytoplankton responses to the 2014–2016 warming anomaly in the northeast
650 subarctic Pacific Ocean, *Limnol. Oceanogr.*, 64, pp. 515-525, doi:10.1002/lno.11056, 2018.
- 651 [Rayner, N. A., Parker, D. E., Horton, E. B., Folland, C., Alexander, L., Rowell, D., Kent, E., and Kaplan, A.: Global analyses
652 of sea surface temperature, sea ice, and night marine air temperature since the late nineteenth century, *J. Geophys. Res.*, 108,
653 4407, doi:10.1029/2002JD002670, 2003.](#)
- 654 Reagan, J. R., Seidov, D., Wang, Z., Dukhovskoy, D., Boyer, T. P., Locarnini, R. A., Baranova, O. K., Mishonov, A. V.,
655 Garcia, H. E., Bouchard, C., Cross, S. L., and Paver, C. R.: World Ocean Atlas 2023, Volume 2: Salinity, A. Mishonov,
656 Technical Editor, NOAA Atlas NESDIS 90, doi:10.25923/70qt-9574, 2024.
- 657 [Reynolds, R. W., Smith, T. M., Liu, C., Chelton, D. B., Casey, K. S., and Schlax, M. G.: Daily high-resolution-blended analyses
658 for sea surface temperature, *J. Climate*, 20, 5473–5496, doi:10.1175/2007JCLI1824.1, 2007.](#)
- 659 Siedlecki, S. A., Pilcher, D. J., Hermann, A. J., Coyle, K., and Mathis, J.: The Importance of Freshwater to Spatial Variability
660 of Aragonite Saturation State in the Gulf of Alaska, *J. Geophys. Res.-Oceans*, 122, 8482–8502, doi:10.1002/2017JC012791,
661 2017.
- 662 Smale, D. A., Wernberg, T., Oliver, E. C. J., Thomsen, M., Harvey, B. P., Straub, S. C., Burrows, M. T., Alexander, L. V.,
663 Benthuisen, J. A., Donat, M. G., Feng, M., Hobday, A. J., Holbrook, N. J., Perkins-Kirkpatrick, S. E., Scannell, H. A., Sen

- 664 Gupta, A., Payne, B. L., and Moore, P. J.: Marine heatwaves threaten global biodiversity and the provision of ecosystem
665 services, *Nat. Clim. Change*, 9, 306–312, doi:10.1038/s41558-019-0412-1, 2019.
- 666 Stock, C. A., Dunne, J. P., and John, J. G.: Global-scale carbon and energy flows through the marine planktonic food web: An
667 analysis with a coupled physical–biological model, *Prog. Oceanogr.*, 120, 1–28, doi: 10.1016/j.pocean.2013.07.001, 2014.
- 668 Suryan, R. M., Arimitsu, M. L., Coletti, H. A., Hopcroft, R. R., Lindeberg, M. R., Barbeaux, S. J., Batten, S. D., Burt, W. J.,
669 Bishop, M. A., Bodkin, J. L., Brenner, R., Campbell, R. W., Cushing, D. A., Danielson, S. L., Dorn, M. W., Drummond, B.,
670 Esler, D., Gelatt, T., Hanselman, D. H., Hatch, S. A., Haught, S., Holderied, K., Iken, K., Irons, D. B., Kettle, A. B., Kimmel,
671 D. G., Konar, B., Kuletz, K. J., Laurel, B. J., Maniscalco, J. M., Matkin, C., McKinstry, C. A. E., Monson, D. H., Moran, J.
672 R., Olsen, D., Palsson, W. A., Pegau, W. S., Piatt, J. F., Rogers, L. A., Rojek, N. A., Schaefer, A., Spies, I. B., Straley, J. M.,
673 Strom, S. L., Sweeney, K. L., Szymkowiak, M., Weitzman, B. P., Yasumiishi, E. M., and Zador, S. G.: Ecosystem response
674 persists after a prolonged marine heatwave, *Sci. Rep.*, 11, 6235, doi:10.1038/s41598-021-83818-5, 2021.
- 675 Takahashi, T., Sutherland, S. C., Wanninkhof, R., Sweeney, C., Feely, R. A., Chipman, D. W., Hales, B., Friederich, G.,
676 Chavez, F., Sabine, C., Watson, A., Bakker, D. C., Schuster, U., Metzl, N., Yoshikawa-Inoue, H., Ishii, M., Midorikawa, T.,
677 Nojiri, Y., Körtzinger, A., Steinhoff, T., Hoppema, M., Olafsson, J., Arnarson, T. S., Tilbrook, B., Johannessen, T., Olsen, A.,
678 Bellerby, R., Wong, C., Delille, B., Bates, N., and de Baar, H. J.: Climatological mean and decadal change in surface ocean
679 pCO₂, and net sea–air CO₂ flux over the global oceans, *Deep-Sea Res. Pt. 2*, 56, 554–577, doi:10.1016/j.dsr2.2008.12.009,
680 2009.
- 681 Tsujino, H., Urakawa, S., Nakano, H., Small, R. J., Kim, W. M., Yeager, S. G., Danabasoglu, G., Suzuki, T., Bamber, J. L.,
682 Bentsen, M., Böning, C. W., Bozec, A., Chassignet, E. P., Curchitser, E., Dias, F. B., Durack, P. J., Griffies, S. M., Harada,
683 Y., Ilicak, M., Josey, S. A., Kobayashi, C., Kobayashi, S., Komuro, Y., Large, W. G., Sommer, J. L., Marsland, S. J., Masina,
684 S., Scheinert, M., Tomita, H., Valdivieso, M., and Yamazaki, D.: JRA-55 based surface dataset for driving ocean-sea-ice
685 models (JRA55-do), *Ocean Model.*, 130, 79–139, doi:10.1016/j.ocemod.2018.07.002, 2018.
- 686 Yang, B., Emerson, S. R., and Peña, M. A.: The effect of the 2013–2016 high temperature anomaly in the subarctic Northeast
687 Pacific (the “Blob”) on net community production, *Biogeosciences*, 15, 6747–6759, doi: 10.5194/bg-15-6747-2018, 2018.
- 688 Wyatt, A. M., Resplandy, L., and Marchetti, A.: Ecosystem impacts of marine heat waves in the northeast Pacific,
689 *Biogeosciences*, 19, 5689–5705, doi:10.5194/bg-19-5689-2022, 2022.
- 690